BNL-209534-2018-JAAM

Energetics of Lithium Insertion into Magnetite, Defective Magnetite, and Maghemite

C. N. Lininger, M. S. Hybertsen

To be published in "Chemistry of Materials"

October 2018

Center for Functional Nanomaterials

Brookhaven National Laboratory

U.S. Department of Energy

USDOE Office of Science (SC), Basic Energy Sciences (BES) (SC-22)

Notice: This manuscript has been authored by employees of Brookhaven Science Associates, LLC under Contract No. DE-SC0012704 with the U.S. Department of Energy. The publisher by accepting the manuscript for publication acknowledges that the United States Government retains a non-exclusive, paid-up, irrevocable, world-wide license to publish or reproduce the published form of this manuscript, or allow others to do so, for United States Government purposes.

DISCLAIMER

This report was prepared as an account of work sponsored by an agency of the United States Government. Neither the United States Government nor any agency thereof, nor any of their employees, nor any of their contractors, subcontractors, or their employees, makes any warranty, express or implied, or assumes any legal liability or responsibility for the accuracy, completeness, or any third party's use or the results of such use of any information, apparatus, product, or process disclosed, or represents that its use would not infringe privately owned rights. Reference herein to any specific commercial product, process, or service by trade name, trademark, manufacturer, or otherwise, does not necessarily constitute or imply its endorsement, recommendation, or favoring by the United States Government or any agency thereof or its contractors or subcontractors. The views and opinions of authors expressed herein do not necessarily state or reflect those of the United States Government or any agency thereof.

Energetics of Lithium Insertion into Magnetite, Defective Magnetite, and Maghemite

Christianna N. Lininger[a], Christina A. Cama[b,#], Kenneth J. Takeuchi[b,c], Amy C. Marschilok[b,c,d], Esther S. Takeuchi[b,c,d], Alan C. West[a,e], Mark S. Hybertsen[f,]*

[a]Department of Chemical Engineering, Columbia University, New York, NY, 10027, United States

[b]Department of Chemistry, Stony Brook University, Stony Brook, NY, 11794, United States

[c]Department of Materials Science and Chemical Engineering, Stony Brook University, Stony Brook, NY, 11794, United States

[d]Energy and Photon Sciences Directorate, Brookhaven National Laboratory, Upton, NY, 11973, United States

[e]Department of Earth and Environmental Engineering, Columbia University, New York, NY, 10027, United States

[f]Center for Functional Nanomaterials, Brookhaven National Laboratory, Upton, NY, 11973, United States

[#] Current address: Department of Chemistry, St. Cloud State University, St. Cloud, MN 56301-4498

ABSTRACT

At low concentrations of lithium insertion into inverse spinel magnetite Fe_3O_4, a phase change to rocksalt-like $Li_xFe_3O_4$ has been observed. We used density functional theory based (DFT) calculations to study the structural origins of this phase change, the concentration at which it occurs, the role of iron vacancies, and the stability of the various motifs that form during the

electrochemical reduction process in the Li-Fe-O ternary space up to x=1.33. We compared our results to new experimental measurements of the open circuit voltage for 8-9 nm magnetite particles over a comparable range of lithium insertion. Of the vacant sites in magnetite (16c, 8b, and 48f) lithium insertion was found to be most stable on 16c. Coulomb interactions between the added lithium and iron at the 8a site in magnetite led to substantial displacement of the iron. As further lithium was added, the most energetically favored motif involved lithium clustering in 16c sites around the shifted 8a iron up to a total of three lithiums. In competition with the lithium clustering motif, lithium insertion could be accompanied by the full displacement of all 8a iron to 16c sites, to form the rocksalt-like $Li_xFe_3O_4$, saturating at x=1. The defective rock-salt structure was found to be more stable than the lithium clustering motif for $x \geq 0.5$. The rocksalt-like $LiFe_3O_4$ was found to be stable in the Li-Fe-O ternary space for a continuous range of Li-Fe organization on the 16c sites, stabilized by Coulomb interactions. For x<1, neither the lithium clustering motif, nor the defective rock-salt like structure for $Li_xFe_3O_4$ were stable against phase segregation to $LiFe_3O_4$ and Fe_3O_4. This phase segregation ($0<x<1$) occurred at a predicted voltage of ~2.0 V. However, when iron vacancies on the 16d site were introduced, lithium insertion to those vacant 16d sites in $Fe_{2.875}O_4$, and γ-$Fe_{2.67}O_4$ (maghemite) resulted in stable intercalated materials at a predicted voltage of ~3.0 V. Beyond the concentration of such iron vacancy sites, phase segregation was predicted to the rocksalt-like $Li_{1.125}Fe_{2.875}O_4$ and $Li_{1.33}Fe_{2.67}O_4$, again at ~2.0 V. These results were consistent with observed open circuit voltages. Finally, the relative stability for several lithium compositions along the FeO to $LiFeO_2$ tie line in the defective rock-salt structure suggested stable compound formation for a range of lithium-iron compositions, but without long-range order in the cation sublattice, consistent with what has been commonly observed in the literature.

1. INTRODUCTION

There is broad interest in a range of iron oxides as electrode materials for secondary lithium-ion batteries due to their low cost, high abundance, and low toxicity.[1–5] Magnetite (Fe_3O_4), hematite (α-Fe_2O_3), maghemite (γ-Fe_2O_3), and α-$LiFe_5O_8$ have been investigated as electrode materials since the 1980s.[6–13] Magnetite specifically, undergoing both intercalation and conversion reactions, has a theoretical capacity of 926 mAh/g against Li^0, corresponding to eight lithium cations inserted per formula unit. However, due to the close packed inverse spinel crystal structure, solid state mass-transfer resistances can lead to poor active material utilization and the inability to reach the theoretical capacity at nominal rates. While the use of nano-scale active material has been extensively investigated to improve capacity and other characteristics, the choice of the matrix, processing of the composite, the occurrence of side reactions, and irreversibility upon charging can all be significant.[14–23] Fundamental understanding of lithiation pathways, optimization of nanostructured active material, and the interplay with the matrix all remain as significant challenges to be addressed through in-depth characterization and multi-scale modeling.[5,22,24–32]

Magnetite has an inverse spinel structure ($Fd\bar{3}m$) with the oxygen atoms forming a face-centered cubic close-packed lattice and the iron atoms occupying specific interstitial sites relative to that lattice, octahedral 16d and tetrahedral 8a, as visualized in Fig 1. If instead, iron atoms occupied all of the octahedral sites (16c and 16d), the result would be wüstite (FeO) with a rock-salt structure. In Fe_3O_4, the iron is nominally mixed valence. In the cubic eight formula unit cell, eight Fe^{3+} cations occupy tetrahedral sites (A-type) while eight each of Fe^{2+} and Fe^{3+} occupy octahedral sites (B-type).[33] This can be expressed as $(Fe_1^{3+})_{8a}(Fe_1^{3+}Fe_1^{2+})_{16d}(O_4^{2-})_{32e}$. Robust

ferrimagnetic order results from antiferromagnetic coupling between A and B type cations. There remain possible competing structures corresponding to the distribution of Fe^{2+} and Fe^{3+} on the 16d site. Also, for the Fe^{2+} ions in an octahedral environment, the extra d-electron occupies three-fold degenerate t_{2g} orbitals that can result in distortions due to the Jahn-Teller effect. Below the Verwey transition at ~120 K, orbital and charge ordering emerge together with structural distortions, the detail of which has been determined surprisingly recently.[34,35] The orbital and charge degrees of freedom represent a complex space with implications for the entropy change at the Verwey transition[33,36] and the interplay of competing, low symmetry structures that ultimately determine the low temperature phase.[37–39]

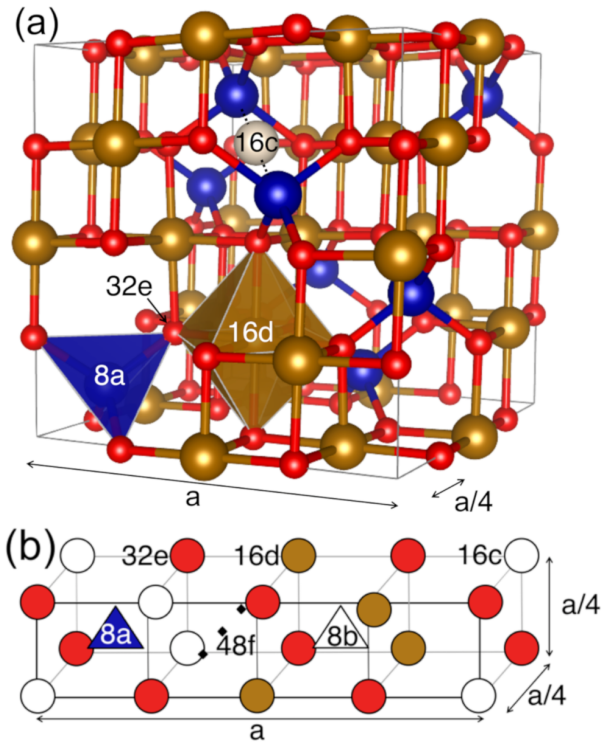

Figure 1. Cubic inverse spinel structure for magnetite, Fe_3O_4. (a) Cubic eight formula unit cell with iron in 16d octahedral sites (brown), iron in tetrahedral 8a sites (blue), and oxygen on 32e (red) forming a cubic close packed lattice to which the octahedral and tetrahedral sites refer. A single, vacant 16c site has been depicted in white to show equidistance to 8a sites. (b) Schematic representation of one quarter of the cubic unit cell indicating further Wyckoff positions.

Guided by nominal ionic charges on the near neighbors, the empty octahedral 16c sites are most attractive for an additional charge, followed by the lower symmetry 48f sites. However, insertion of Li^+ onto an octahedral 16c site exposes it to two, nearest-neighbor nominally Fe^{3+} cations (Fig. 1). Thackeray, *et al.*, applied this picture to develop their hypothesis for the structural response upon lithiation.[7] At low levels of lithiation, below a critical concentration (x_c) this repulsion would be accommodated locally. The natural outlet for the perturbed local Fe^{3+} on 8a sites drives them toward nearby empty 16c sites. Since each 16c site has two 8a neighbors, local displacement of Fe^{3+} to 16c sites sets up a cascade of cation shifts. Above x_c, a concerted shift of Fe^{3+} from 8a to 16c sites would occur, resulting in a rocksalt-like structure with partial occupancy $(Li_xFe)_{16c}$, $x_c<x<1$. This picture was supported by simulations based on empirical interaction potentials.[12] The simulations also suggested that, for low levels of lithiation, up to three Li^+ would cluster together instead of being randomly dispersed.

To give a frame of reference for discussion of lithiation of magnetite, a Li–Fe–O ternary convex hull is shown in Fig. 2, primarily based on data from the Materials Project. The stable phases shown are all known compounds (SI S.4).[40] We add α-$LiFe_5O_8$, also known from experiment.[9,11,41] The dashed line illustrates the continuous insertion of lithium into Fe_3O_4 to form $Li_xFe_3O_4$, with some discrete possible compounds indicated for x=1, 2, 4, 5, and 8 at tie line intersections. The stability of any phases along this line, thermodynamically or kinetically, is fundamental to understanding the insertion process. For segments along this line where the phases are unstable, absent kinetic limitations, each successive Gibbs triangle in Fig. 2 defines phase segregation products. The corresponding electrochemical open circuit voltage consists of a series of plateaus.

For x>1, this would involve formation of Fe^0 and a sequence of intermediate phases leading to final conversion to Li_2O.

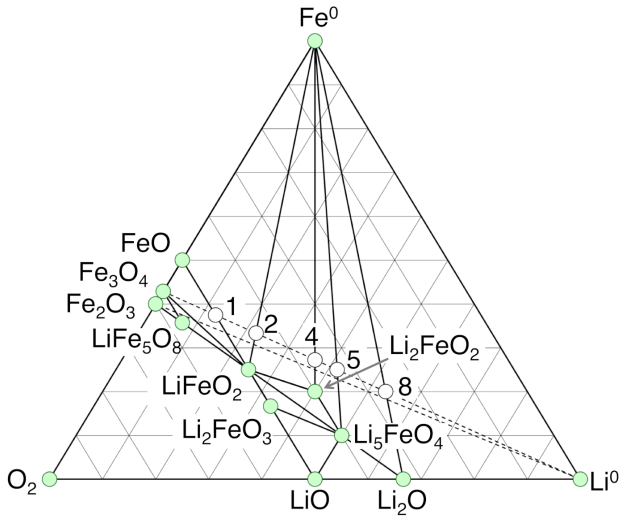

Figure 2. Li-Fe-O ternary phase diagram. The green points show observed phases. Dashed lines are lithium intercalation lines. White points and corresponding numbers are reference points for x in $Li_xFe_3O_4$.

Early experiments showed a continuous variation in open circuit voltage starting from about 3 V, with a change in slope near x=1 and finally leveling off to a plateau value of 1 V for x>1.5.[42] Analysis of X-ray diffraction revealed the change to a rock-salt structure noted above. For x>1, this nominally requires Li^+ to occupy sites in addition to 16c, such as 8b or 48f. Even so, evidence pointed to a rock-salt structure for $Li_2Fe_3O_4$ with the possible presence of unreacted spinel Fe_3O_4 regions, although details of the lithium cation positions could not be determined.[10,43] Complimentary support was the lack of evidence for Fe^0 formation. Finally, the long plateau for larger x suggested direct conversion to Fe^0 and Li_2O, without evidence for intervening phases.

Subsequent research, including that based on nano-scale magnetite crystallites, agreed on the appearance of the rock-salt structure, although the corresponding range of x varied.[20,24,28,30,31]

Direct experimental evidence for the formation of Fe^0 upon electrochemical lithiation was achieved through use of a nano-crystalline Fe_3O_4 material.[30] Studies have been performed that address the slow kinetics of the processes occurring during discharge, revealing that magnetite underwent long relaxation times following lithium insertion, during which parasitic side reactions could occur.[16,27,29] Also, as a function of particle size and discharge rate, multiple reactions could occur simultaneously in a single particle during discharge.[24,44] In particular, real-time transmission electron microscopy, performed at a discharge rate of 0.017 mA/cm^2, clearly showed the coexistence of the different phases in individual, nano-scale particles.[28]

Sample stoichiometry presents an additional complication. Magnetite samples often have some concentration of cation defects depending on synthetic method and oxygen exposure.[33] Iron vacancies specifically, corresponding to $Fe_{3-\delta}O_4$, have been observed, occurring predominantly on the 16d site (in the B-type position), as shown by Mossbauer spectroscopy.[45] The structure of maghemite, γ-Fe_2O_3, presents the logical limit of fully oxidized $Fe_{3-\delta}O_4$ with δ=0.33. The vacancies are generally confined to the 16d site, schematically $(Fe_1^{3+})_{8a}(Fe_{1.67}^{3+}\boxdot_{0.33})_{16d}(O_4^{2-})_{32e}$. Maghemite can be formed by topotactic oxidation of magnetite.[46] Maghemite crystals can be prepared in which the vacancies are ordered in a unit cell that is tripled along one of the Cartesian axes of the conventional magnetite cubic cell to form tetragonal unit cell with space group $P4_12_12$.[47,48] This ordering was confirmed by calculations using classical interatomic potentials, which also pointed to minimization of ionic interactions as the basic mechanism.[49]

Lithiation of maghemite, including in nano-crystalline form, has been extensively studied.[13,15,17,25,26,50,51] Overall, the characteristics are similar to magnetite, including long

relaxation times following lithium insertion, parasitic side reactions, and improved electrochemical performance with nano-sizing. For ease of comparison with magnetite, we describe the results with reference to the equivalent formula unit, $Li_xFe_{2.67}O_4$. Pernet, *et al.*, identified a sequence of three reaction on an electrochemical lithiation path ending at x~1.33.[13] The first reaction corresponded to the filling of 16d vacancies with lithium, ending at about x=0.33. The second reaction, clearly slower, corresponded with clear changes in structure measured by X-ray diffraction, specifically from spinel to rock-salt. At the end of this regime, there was residual tetrahedral Fe and x~1.15 indicated that not all 16c sites were occupied. The third reaction, considerably faster, was hypothesized to correspond to filling those residual sites with lithium. The parallel with the original Thackeray, et al., picture for magnetite is clear. Interestingly, some subsequent investigations of nano-scale materials have suggested a suppression of the transition to the rock-salt structure,[15,26] and observed apparent reversibility in the spinel to rock-salt transition.[17] Other studies showed an irreversible spinel to rock-salt transition.[24,31]

As studies on the lithiation of magnetite progress, the importance of discharge rate on observed mechanism, the observation of slow kinetics of phase change, and mass transport resistances occurring in the material, highlight the importance of separating kinetic from thermodynamic effects. For the initial stages of lithium insertion, a key question controlling the thermodynamic picture is the relative stability of $LiFe_3O_4$. The second question is whether there is finite range of x over which $Li_xFe_3O_4$ forms continuously, an intercalation regime, as suggested by the experimental voltage profiles. Finally, the role of iron vacancies and the extent to which maghemite behaves differently during lithium insertion must be addressed. This is particularly highlighted in nanocrystalline samples. Experiments show that processing conditions may lead to

a structure with magnetite core and an oxidized cladding, Fe^{3+} rich[30] or even specifically maghemite.[52] Overall, fundamental understanding requires open circuit potential data where kinetic factors have been thoroughly characterized so that the regimes of continuous lithium insertion can be distinguished from the plateaus that signal conversion reactions.

In this paper, we present open circuit potential data for magnetite nanocrystalline materials based on slow lithium insertion rates and open circuit potential monitored for up to 30 days. We then present an in-depth analysis of formation energy and open circuit potential, using DFT-based calculations, substantially expanding on the scope of structures considered in recent studies.[28,31] We revisited the relative stability of the rock-salt-like $LiFe_3O_4$ phase and the relative stability more generally of $Li_xFe_3O_4$ at low levels of lithiation, $x<1$. We also considered lithium insertion into iron deficient magnetite, $Fe_{2.875}O_4$, and maghemite, $Fe_{2.67}O_4$. Based on calculations for distinct ways to organize lithium and iron cations on the 16c site of rock-salt-like structures for $LiFe_3O_4$ in an eight formula unit cell, we found a series of structures that were stable relative to the convex hull at zero temperature with a continuous variation in energy. Relative to the most stable $LiFe_3O_4$ structure, we found no stable, intermediate phases for $Li_xFe_3O_4$ with $x<1$. We considered the impact of charge, spin and orbital ordering on our conclusions. The calculations showed that lithium initially inserted into iron vacancies available on 16d sites, including filling all the available such vacancies in maghemite. The predicted voltage for this process, near 3 V, corresponded well to the initial, low lithium concentration measured open circuit potential. The predicted voltage for the spinel to rock-salt-like structure conversion, near 2 V, aligned with the first plateau in the measured open circuit potential. However, the lithium concentration at which

the measured plateau started was beyond that which could be accounted for simply through iron vacancies in the sample.

2. METHODS

2.1. Open Circuit Potential Measurements. Electrochemical testing was done using two-electrode coin cells versus lithium metal electrodes, at 30° C. The 8-9 nm Fe_3O_4 nanoparticles were synthesized by co-precipitation using previously reported methods.[19,53] The cathodes were fabricated using the synthesized magnetite (90%), super P carbon additive (5%), and polyvinylidene fluoride binder (5%) coated onto a copper foil substrate. The electrolyte was formed from dimethyl carbonate and ethylene carbonate in a 70:30 ratio by volume with 1 M $LiPF_6$. Constant current lithiation at C/200 was carried out to x=0.2, 0.4, 0.5, 0.6, 0.8, 1.0, 1.5, and 2.0. Subsequent voltage monitoring under open circuit conditions for up to 30 days was performed.

2.2 First Principles Calculations. DFT-based calculations were performed with the Vienna *ab initio* simulation package (VASP),[54,55] using the projector augmented wave (PAW) method.[56] The generalized-gradient approximation in the form proposed by Perdew, Burke and Ernzerhof (PBE) was used for the exchange-correlation potential.[57] To approximately account for local Coulomb interactions in the Fe 3*d* orbitals, the DFT+U approach was used,[58,59] specifically in the spherical approximation.[60] In this case there is only one parameter, taken to be U_{eff}=5.3 eV for all Fe 3*d* orbitals, independent of nominal local ionic configuration.[40] Spin polarized calculations were performed throughout.

The plane-wave basis set was determined by a cutoff of 600 eV, chosen following tests to assure reliable relaxation of unit cell parameters based on the computed stress tensor. The reference unit cell was chosen to be the simple cubic form of the inverse spinel structure with eight formula units per cell. Where indicated, other unit cells were used. For maghemite, $Fe_{2.67}O_4$, the $P4_12_12$ structure in a 3×1×1 supercell, relative to the cubic reference, was adopted from the prior theoretical study and consistent with experiment.[49] For the reference eight formula unit Fe_3O_4 cell, the Brillouin zone sampling was done with a Γ-centered grid defined by a 3×3×3 mesh and using the Methfessel-Paxton smearing scheme of order 1 with broadening parameter 0.2 eV.[61] Sampling was adapted for other cells to be equivalent as is shown in Supplementary Information (SI), Table S1. In cases where self consistency with specific d-orbital occupancy for Fe^{2+} centers was hard to achieve, a sequence of electronic minimizations was employed. First in a Gaussian broadening scheme, the broadening parameter was reduced in steps to a much smaller value (0.01 eV) with a small or zero value of U. Then the U was incremented in steps to the final value.[62]

Explicit tests indicate that these choices of energy cutoff and k-point sampling grid give total energies with convergence to about 2 meV/f.u. In general, unit cells were optimized without imposing symmetry and relaxation was carried out to an explicit force criterion of 0.05 eV/Å. For auxiliary compounds, results were similarly converged with respect to k-point sampling.

In the literature, there has been a range of chosen values of U_{eff} for magnetite, U_{eff} = 3.7-5.3 eV.[40,63,64] To probe the impact of U_{eff} on formation energy here, the reaction $0.5LiFe_3O_4 + 0.5\ Fe_3O_4 \rightarrow Li_{0.5}Fe_3O_4$, was calculated as a function of U_{eff} in the range 0.0 to 7.0. In the range of U_{eff} = 4.5-5.7, the formation energy was found to plateau, the details of which can be seen in the SI,

Fig. S1. Our final results should not be too sensitive to the choice of U_{eff} =5.3 eV from the Materials Project.

The assignment of the nominal ionic charge for discussion and analysis was based on local magnetic moment, that for Fe^{2+} being clearly distinguishable from that for Fe^{3+}. For analysis purposes, nominal ionic charges and computed, relaxed structures were used with the MADEL program from the RIETAN-FP-VENUS package to compute Madelung energies.[65] Crystal structures were visualized using the VESTA package, which was also used to create figures with atomic structure depicted herein.[66] The estimated local magnetic moments were obtained from VASP with the option chosen to perform local projections to the localized projector functions defined in the PAW method. No local radial cutoff needs to be specified in this case. As noted in a prior study, the moments were well localized, with minimal moments found for oxygen centered spheres.[49]

The lowest energy spin configuration calculated for Fe_3O_4 was ferrimagnetic, driven by antiferromagnetic coupling between iron ions on tetrahedral 8a sites and those on octahedral 16d sites. Local magnetic moments showed Fe^{3+} (4.2 μ_b) on 8a sites and an even mixture of Fe^{3+} (4.3 μ_b) and Fe^{2+} (3.7 μ_b) on 16d sites. The net magnetic moment was 3.96 μ_b per f.u. including small, but non-zero magnetization on oxygen sites. The low temperature saturation magnetization for Fe_3O_4 has been measured to be 4.05 μ_b/f.u.[67] We note that low spin solutions are also possible for Fe^{2+}, and have previously been investigated at high pressures.[68] Based on the clear emergence of the high spin solution in the calculations for near ambient conditions and the good agreement with experiment, we have not investigated low spin solutions in this study.

In the rock salt structure, the experimental reference FeO compound (monoclinic a=5.2615 Å, b=3.0334 Å, c=3.0602 Å, with β=124.649°) is antiferromagnetic with ordering along the [111] direction.[69,70] Experiments and DFT-based calculations have been modeled using a near-neighbor Heisenberg model.[71] The nearest neighbor Fe-Fe exchange constant J_1 (coupling through oxygen octahedral edges) was relatively weak compared to the second neighbor J_2 (coupling through corner shared oxygen with a 180° angle). Our calculations, allowing for further distortion and relaxation in a four formula unit cell monoclinic cell taken from experiment,[70] resulted in local magnetic moments showing Fe^{2+} moments alternating $\pm$3.7 μ_b on [111] planes and a resulting net magnetic moment of 0.0 μ_b per f.u., with a=5.4481 Å, b=3.0222 Å, c=3.1146 Å, and β=124.6309°.

For the reference compound $LiFeO_2$, the α-$Li_2Fe_2O_4$ cubic phase with cation disorder on the 16c and 16d Wykoff sites from the Fd$\bar{3}$m space group, $[Li_3Fe_1]_{16c}[Li_1Fe_3]_{16d}[O_8]_{32e}$, was computed to be 0.54 meV/atom lower than the cation-ordered phase, $[Li_4]_{16c}[Fe_4]_{16d}[O_8]_{32e}$. It was also found to be 16 meV/atom lower in energy than the competing, γ-tetragonal phase.[72] Cation disorder was tested in a two formula unit cell with nine symmetry unique ways to enumerate four lithium and four Fe cations on the 8 16c + 16d sites. Ferromagnetic coupling within [111] planes and antiferromagnetic coupling between them was found to be lowest in energy, as found in experiment,[73] with magnetic moments $\pm$4.3 μ_b. The roles of chemical, charge and orbital ordering will be discussed next. A summary of our computed structure properties for the reference compounds in this study appears the SI, Table S2.

2.3 Sampling Configurations for Lithium Insertion. The site-occupancy disorder (SOD) tool[74] and pymatgen tool from the Materials Project[75,76] were used to determine the symmetry distinct

number of configurations to sample for each structure in which specific Wyckoff positions were either partially occupied or had mixed occupation.

Consider the case of $Li_xFe_3O_4$ as an example. In a two formula unit, spinel unit cell ($Fd\bar{3}m$ space group) up to two lithium atoms can be inserted to available 16c sites. For *x*=0.5 (one lithium), there are four total configurations, but just one that is distinct based on the symmetry of the spinel parent. For *x*=1.0 (2 lithium), there is one symmetry distinct configuration out of six. Alternatively, with all of the iron atoms on 8a sites shifted to 16c sites, the parent has a rock-salt structure with half of the iron sites frozen from the 16d sites of spinel and a mixed occupancy of iron, lithium and vacancies on the 16c sites. Continuing to use the Wyckoff positions from the $Fd\bar{3}m$ space group, for *x*=1.0, there is once again one unique configuration out of six possible. However, if the *x*=1.0 case is reconsidered in the $F\bar{3}m$ space group, with only one cation site for all of the lithium and iron, then there are four unique structures.

As the supercell size is increased, a more refined mesh of composition values can be studied, but the number of configurations grows rapidly. We focused on an eight formula unit cell derived from the cubic, room temperature magnetite structure. We represented both the spinel and the rocksalt structures in the $Fd\bar{3}m$ space group. Based on the simplest possible physical model of lithium insertion, the full occupancy of the 16d site was maintained (no atomic exchanges with lithium considered) and lithium insertion was restricted to the 16c site. We then compared two scenarios: (1) the tetrahedral iron was relaxed locally in response to the lithium insertion; and (2) the tetrahedral iron was collectively displaced to 16c sites. The number of configurations, both raw and symmetry distinct, are enumerated in the SI, Table S3.

In scenario one, insertion to the spinel phase, all symmetry distinct configurations were calculated for the sequence of concentrations from x=0.125 through 0.625, at which point these structures were relatively high in energy. For the stoichiometric case of x=1.0, all 97 distinct configurations were also sampled. However, in scenario two with x=n/8 < 1.0, eight iron, n lithium, and (8-n) vacancies occupied the 16c sites. The number of symmetry distinct configurations exploded. For this scenario, we used physically motivated sampling. Starting from a specific configuration for x=1, calculations were done for all symmetry distinct ways to form one lithium vacancy in the $LiFe_3O_4$ parent rock-salt structure to make $Li_{0.875}Fe_3O_4$. The lowest energy $Li_{0.875}Fe_3O_4$ result was then used as the next rock-salt parent, and all the symmetry unique ways to introduce a second lithium vacancy was sampled to make $Li_{0.75}Fe_3O_4$. This sequence was continued to lower lithium concentrations as needed. To assess the robustness of this limited sampling, we repeated it for several configurations chosen from the set of 97 available for the $LiFe_3O_4$ parent rock-salt structure, rank ordered according to increasing energy. Those chosen were 1st, 2nd, 3rd, 10th, 20th, 30th, and 97th. The formation energies (SI, Fig. S2) suggest that this limited sampling gave reliable physical conclusions.

In the study of the effect of iron vacancies, the low lithium concentration cases were considered following the analogue of scenario one, considering all symmetry distinct configurations. At the opposite limit of full lithium insertion, the lowest energy x=1.0 rock-salt parent structure was used to introduce iron vacancies on 16d. Iron at a single site was exchanged for a lithium. This was repeated for all 16d irons to sample possible configurations for $Li_{1.125}Fe_{2.875}O_4$, since the parent had P_1 symmetry. The maghemite cell with 24 formula units was too large to sample configurations systematically.

2.4 Charge and Orbital Order. The DFT calculations inherently probe the zero-temperature structure. In the case of magnetite, this includes the impact of Jahn-Teller distortions around the Fe^{2+} centers and the ordering of the distribution of Fe^{2+} and Fe^{3+} among 16d sites. In a local picture, the distortion is specifically linked to the occupied spin down d-orbital on each Fe^{2+} site among the Jahn-Teller split t_{2g} manifold of d-states. In principle, for n formula units being sampled, there is a combinatorial factor for charge order multiplied by 3^n for orbital selection on the n Fe^{2+} sites. In practice, the lattice connectivity makes the local distortions interdependent and electronic band formation competes with the localization of the d-electrons. The problem is quite complex.

Several groups have used DFT calculations to study charge and orbital orderings in different space group representations and supercell sizes for Fe_3O_4.[35,38,39] In this discussion, nominal charge order (Fe^{2+} and Fe^{3+}) was formally distinguished by local magnetic moment and orbital order was determined from local, projected orbital character of spin down energy states on those sites. These correlated with local octahedral volumes and distortions.[34,35] Compared to an ideal, undistorted cubic structure, the largest energy scale (~0.4 eV/f.u.) was associated with allowing distortions of local octahedral and the concomitant distortion of the unit cell and symmetry lowering.[38] A much smaller variation in energy was attributable to different ordering schemes in cells that ranged from four to 16 f.u. Starting from different experimental refinements of the low temperature magnetite structure, DFT calculations exhibited the charge and orbital ordering dictated by the pattern of octahedral distortions. The range of relaxed total energies was ~0.02 eV/f.u.[38] In a different approach, the cluster expansion concept was extended to model the charge-orbital space more extensively.[39] The results showed that structures with the original, Verwey charge order[33,77,78] were competitive with those based on P2/c and Cc experimental

refinements that implied a different charge order. Specifically, structures with Verwey charge order had energies in the middle of the ~0.02 eV/f.u. range found previously.[38] In addition, a new ordering scheme was identified that DFT calculations indicated was a further 0.02 eV/f.u. lower in energy than the previous calculated, lowest energy for a Cc structure. So far as we are aware, these alternative orbital ordering results have not been compared to the latest experimental refinements.[34,35]

The experimental room temperature, Fd$\bar{3}$m cubic structure includes an internal structure distortion parameter u_{iso} = 0.004[43,79] which displaces the oxygen atoms from the high symmetry 32e Wycoff positions. This results in 16c octahedra having larger volume than 16d octahedra but leaves the Fe-O bond lengths equal in each octahedron locally. We used this as a starting point for full relaxation without imposed symmetry. Upon full relaxation, the distribution of the nominal Fe^{2+} and Fe^{3+} cations on the 16d sites was found to be consistent with the Verwey charge order, where planes in the <100> direction alternate between Fe^{2+} and Fe^{3+}. For comparison, we also considered several scenarios. First, the energy gain was 0.389 eV/f.u. when going from the Fd$\bar{3}$m cubic (a=b=c=8.54 Å and $\alpha = \beta = \gamma = 90°$) structure, with u_{iso}=0.0 and all cations fixed at their high symmetry position to the same supercell (a=b=c=8.54 Å and $\alpha = \beta = \gamma = 90°$,) but with internal parameters allowed to relax. This scale agrees with Jeng, Guo, and Huang.[80] Allowing the cell shape to distort to monoclinic (Imma) resulted in a further 0.008 eV/f.u. reduction in energy. We also calculated relaxed structures starting from low temperature P2/c experimental structure with non-Verwey charge order[37,81] and found a minimum energy that was 0.002 eV/f.u. higher than our lowest Fd$\bar{3}$m-based refinement. Visualizations of the structure, charge and orbital order in each case appear in the SI, Fig. S3. Overall, our computed energies for different charge and

orbital orders agree with the tabulation of Zhou and Ceder.[39] Their results suggest that the larger Cc structure (16 fu) based on experiment could be 0.015 eV/f.u. lower than our lowest Fd$\bar{3}$m-based refinement. Further details appear in the SI.

For $LiFe_3O_4$ in rock-salt cells under consideration here with eight lithium and eight iron cations distributed on the 16c sites and 16 iron cations on 16d sites, there still remains the internal organization of 16 Fe^{2+} and eight Fe^{3+} cations. Starting with the oxygen sublattice from the room temperature, cubic Fd$\bar{3}$m magnetite structure with the measured u_{iso}, we again fully relaxed without imposing symmetry. We found Fe^{2+} on 16c sites and an equal mixture of Fe^{2+} and Fe^{3+} on the 16d sites across all 97 unique configurations of considered. This was consistent with the positive u_{iso} imposed, which led to larger octahedra on 16c sites. Considering as an example the lowest energy cation ordering for the $LiFe_3O_4$ structure, the energy gain in going from a u_{iso} of 0.0 to the lowest energy value of u_{iso}=0.004 was small, 0.064 eV/f.u. compared to the energy gain of allowing the internal degrees of freedom to fully relax at fixed cell parameters, (a,b,c,α, β, γ), 0.316 eV/f.u. There was an additional lowering of < 0.001 eV/f.u. for relaxation of cell parameters, a,b,c,α, β, γ. This result was generally true for other cation orderings in $LiFe_3O_4$, where the largest energy scale was the relaxation of the internal degrees of freedom.

While the sequence of energy scales for $LiFe_3O_4$ was similar to what we found for magnetite, the $LiFe_3O_4$ case was inherently different from magnetite in that the lithium cation distribution on the 16c sites already drove a non-uniform electrostatic environment for the 16d sites. The results reported below will show a range of 0.20 eV/f.u. across the sampling of lithium cation configurations, an order of magnitude larger than the charge and orbital ordering scale for magnetite noted above. The treatment of charge order in $LiFe_3O_4$ was also assessed herein. For

each unique ionic order, there was an additional degree of freedom associated with charge order for iron on 16c+16d sites. As it was not computationally feasible to calculate all possible charge orders for each of the 97 unique ionic orders, the energy scale associated with the charge order was probed by varying charge on the 16c vs. 16d sites with the use of the u_{iso} parameter. It was found that the experimental u_{iso} parameter for magnetite generally predicted a lower energy charge order in $LiFe_3O_4$, but in some cases, lower energy charge orders were isolated with an alternate u_{iso} parameter. The details and energetics for the individual test are discussed in Supplementary Section 3 and shown in Fig. S4. The energy scale associated with charge order was found to be 0.033 eV/f.u. in $LiFe_3O_4$, the same scale as was found for magnetite, and again an order of magnitude smaller than the energy scale associated with ionic order in this problem. Further details for charge order analysis in $LiFe_3O_4$ can be seen in Fig. S4. Taken together, these results suggest that the charge order and local Jahn-Teller distortions that emerged self consistently were likely representative of the lowest energy iron cation charge and orbital order, although for each lithium configuration, there may well be several competitive orders possible.

More broadly, for the $Li_xFe_3O_4$ cases, in either spinel or rock-salt, the same overall logic applies and the internal Fe charge and orbital order was not optimized, beyond that which was found self-consistently in fully relaxed calculations.

2.5. Phase Stability and Computation of Open Circuit Potential. The first principles calculations have been used to predict specific electrochemical properties of the materials under study here using a conceptual framework that has been well developed and described in recent reviews.[82–84] More broadly, the use of DFT-based computations to assess material stability and phase diagrams has been embedded in publicly accessible databases, the Materials Project[40] and

the Open Quantum Materials Database.[85,86] The present study was restricted to zero temperature and utilized binary and ternary convex hull constructs to assess stability. Open circuit potential was estimated from total energy differences. Relevant details are briefly summarized below. Where specific materials, *e.g.*, representing a certain concentration *x* of lithium in $Li_xFe_3O_4$, could adopt different arrangements, a representative range of configurations was sampled, as described in the previous subsection.

The stable phases in an insertion reaction with a nominally fixed host and a single degree of freedom were determined by the convex hull of the lowest formation energies as a function of composition calculated relative to the end-point compounds, *e.g.*,

$$E_F = E(Li_xFe_3O_4) - xE(Li_1Fe_3O_4) - (1-x)E(Fe_3O_4) \quad (1)$$

These energies were reported per host formula unit. For a composition range [x_1, x_2] bounded by two stable phases, open circuit voltage associated to the conversion process in this range was determined by the free energy difference between the end points relative to the lithium metal reservoir. This was approximated by the zero temperature energy difference, *e.g.*,

$$V = -\frac{E(Li_{x2}Fe_3O_4) - E(Li_{x1}Fe_3O_4) - (x_2 - x_1)E(Li)}{(x_2 - x_1)F} \quad (2)$$

where *F* is Faraday's constant. Even in a composition range where the open circuit potential may vary continuously, in practice, the composition x was sampled discretely, based on the choice of supercell size. The open circuit potential was approximated by finite differences of the same form as Eq. (2).

For the full ternary stability analysis, the formation energies were computed relative to the constituents in standard states (bcc iron, bcc lithium, and molecular oxygen) and reported per

atom for each compound. In the ternary convex hull, such as illustrated in Fig. 2, the test for an additional stable phase was that its formation energy be negative relative to decomposition into the nearest neighbor stable phases. For a continuous line across the phase diagram, such as that illustrating lithium insertion into Fe_3O_4 in Fig. 2, the zero temperature result for the corresponding open circuit voltage, assuming equilibrium among all possible products at each point along the path, was a series of constant values, one for each of the Gibbs triangles traversed.

Shortcomings in the accuracy of the DFT+U approach for formation energies of compounds have been documented in the literature, with different empirical remedies suggested.[64,87–89] To improve the predictions based on the DFT+U approach, two types of empirical corrections are included in results returned from queries to the Materials Project. First, an overall offset in transition metal oxidation energies can be addressed by adjusting the oxygen reference energy.[64]

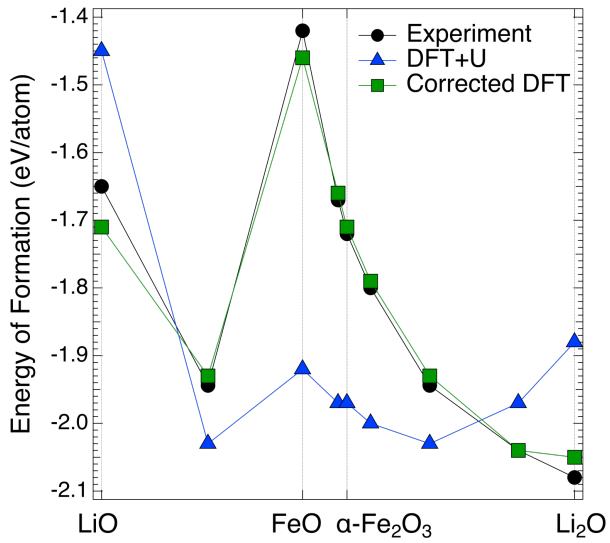

Figure 3. Accuracy of the computed formation energies of phases in the Li-Fe-O phase diagram. Interior phases are considered following a path through the ternary phase diagram traversing LiO → FeO → Fe_2O_3→ Li_2O with distance on the x-axis proportional to distance on the ternary phase diagram. Li_2FeO_3 was not included while $LiFeO_2$ appears twice as a crossing point in the path traversed. Measured results are compared to those based on DFT+U as computed and with the inclusion of specific corrections for the energy of O_2 in DFT[64] and for oxidation of iron in DFT+U[86], as discussed in the text.

Second, it has been argued that while the DFT+U approach is more accurate for transition metal oxides, the conventional PBE approach is more accurate for the metals themselves.[87] This has been addressed with a correction applied to each transition metal for which a finite U is applied in the oxide and determined from experimental formation energies. We have analyzed these two corrections using the known experimental formation energies for FeO, Fe_3O_4, α-Fe_2O_3, α-$LiFeO_2$, LiO, Li_2O, Li_5FeO_4, and $LiFe_5O_8$ within the Li – Fe – O ternary phase diagram (Fig. 2).[85,86,90–93] The details appear in the SI, including the determination of the correction applied for iron upon changes in formal oxidation state that depends on the value of U chosen. Figure 3 illustrates the impact of the corrections on the formation energies following a path through part of the phase diagram. The energies are tabulated in the SI, Table S4. Generally, the stability criterion itself is not affected, but the open circuit voltage is changed for processes in which Fe^0 is a reaction product.

3. RESULTS AND DISCUSSION

3.1. Measured Reversible Potential. Galvanostatic intermittent titration technique experiments (GITT) at x = 0.2, 0.4, 0.5, 0.6, 0.8, 1.0, 1.5, and 2.0 equivalents of lithium into 8-9 nm Fe_3O_4 nanoparticles resulted in the voltage relaxation curves shown in Fig. 4a. The increase and subsequent decrease in potential for x = 0.5 in Fig. 4a has been previously examined and attributed to side-reaction in a similar magnetite system.[29] Notably, previous study of Fe_3O_4 samples prepared by the coprecipitation technique indicated that the average oxidation of the materials was influenced by the crystallite size where the average oxidation state was higher for smaller crystallite samples.[94] This observation is consistent with a defect structure with a higher iron oxidation state at the surface. It was observed that at low depths of discharge (x = 0.2 and 0.4),

the relaxation profiles took 30 days to reach full equilibrium. For more extensive discharge (x = 0.6, 0.8, 1.0, 1.5, and 2.0), ~5 days was sufficient relaxation time. Previous studies have shown that for larger particles, 30 days relaxation time may not be sufficient.[27] In Fig. 4b, the reversible potential starts with a concentration dependent region that lasts until x = 0.8 and ranges from 2.8 V down to 1.9 V. Following the concentration dependent intercalation regime, there is a short voltage plateau near x = 1.0 followed by a slight drop in voltage out to x = 2.0. In comparison, the early measurements by Thackeray, et al., were based on shorter equilibration time (24 hours).[7,42] The low concentration reversible potential was similar to that measured here, but the plateau region was less pronounced near x=1 and had a lower voltage.

3.2. Structure and Stability of $LiFe_3O_4$. The formation of the widely observed $LiFe_3O_4$ rocksalt structure by lithium insertion to the spinel Fe_3O_4 can be decomposed into elementary steps to analyze the energy contributions. This was calculated in a two formula unit cell maintaining ferrimagnetic order from the spinel parent. The first step, shown in Fig. 5, was the movement of all 8a iron to 16c sites with no change in lattice parameter from the x=0.0 structure, but allowing relaxation of internal coordinates. The energy cost to displace the iron from 8a to 16c was found to be +1.48 eV/f.u. Second, the structure was expanded to the final x=1.0 lattice parameter, representing the energetic cost of lattice expansion, found to be negligible (Fig. 5). The third step was the energy gain associated with lithium insertion from metallic lithium into the defective rocksalt structure, which was found to be -1.80 eV/f.u from the starting structure. These results highlight two physical aspects of the lithiation process in magnetite. First, the Coulomb stabilization of the inverse spinel structure in comparison to the defective rock-salt structure is quite large. Second, the direct insertion of lithium from the metal into an available octahedral

vacant site in the defective rock-salt structure is even larger. Also, the net of the energetics suggests a clear driving force to form the stoichiometric $LiFe_3O_4$.

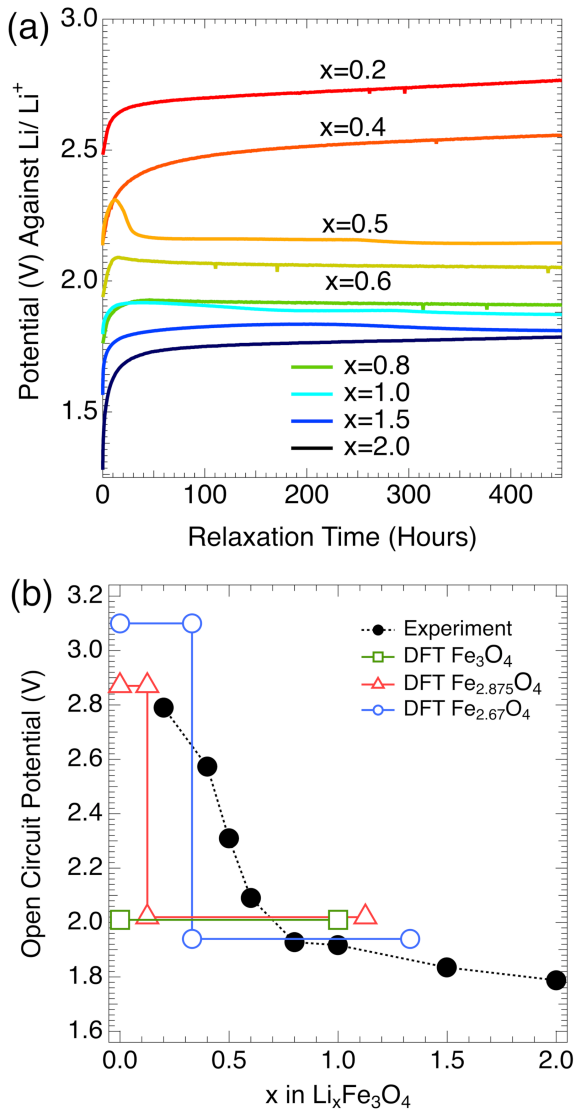

Figure 4. Measured and computed voltages. (a) Voltage relaxation curves for lithiation of 8-9 nm Fe_3O_4 nanoparticles measured by GITT. (b) Reversible potential as a function of lithium concentration. Experiment based on the long time limit of the voltage in the GITT experiments for $0 < x < 2$. DFT predicted voltage profiles for lithiation of pristine magnetite Fe_3O_4 (green squares), defective magnetite $Fe_{2.875}O_4$ (red triangles), and maghemite $Fe_{2.67}O_4$ (blue circles).

To probe the detailed structure and stability of $LiFe_3O_4$, fully relaxed structures and energies were computed for 97 symmetry distinct configurations in an eight formula unit cell, as

described in Sect. 2.3. The computed formation energies relative to FeO and $LiFeO_2$ are displayed in Fig. 6a. For comparison, the one symmetry unique configuration in a two formula unit cell was included. As described in Sect. 2.4, the set of 97 configurations all have Fe^{3+} on the 16c sites. The lowest energy structure from this set is visualized in the SI, Fig. S4b. An alternative charge ordering among the eight Fe^{3+} and 16 Fe^{2+} on 16c and 16d sites in the eight formula unit was also considered for a subset of the 97 configurations, as described in Sect. 2.4. Interestingly, this prescription, when applied to the configuration in Fig. S4b, resulted in an alternate charge order that was found to be even lower in energy (Fig. 6a). It is visualized in Fig. 7a and a structural file is included in Supplementary Information Section 5. However, the formation energies for the other structures sampled to probe the impact of alternative charge order, shown in the SI (Fig. S4c), did not result in any other structures that were competitive as the lowest energy structure. Further details are presented in the SI. In particular, the change in energy associated with the alternative charge ordering was found to be ~0.03 eV/f.u., substantially smaller than the dynamic range in Fig. 6a.

Across the sampled configurations, the major factor was the arrangement of lithium and iron on the 16c sites, and the energy varied by ~25 meV/atom or 0.20 eV/f.u. When translated to the electrochemical potential scale for lithium insertion, this range corresponds to 0.13 V variation. This demonstrates concretely that the energy scale associated with charge ordering among the iron cations in $LiFe_3O_4$ is an order of magnitude larger than that for pure magnetite (0.02 eV/f.u.).[39,80] Each configuration of lithium occupancy of the 16c sites leads to a different electrostatic driving force to which the distribution of iron cations responds. To assess this further, the Madelung energy for each fully relaxed structure was computed with the formal charge assigned to each ion based on the final computed electronic structure, as described in Sect. 2.2.

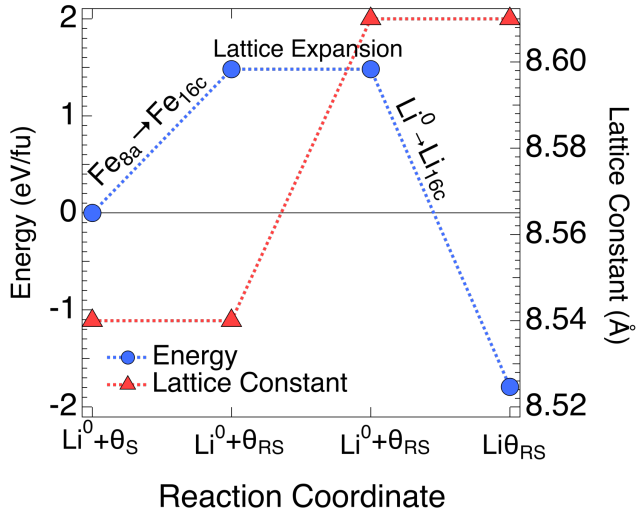

Figure 5. Stepwise energetic contributions to form $LiFe_3O_4$ in the rock-salt phase from lithium metal and spinel Fe_3O_4. Step 1: Starting in the inverse spinel phase (designated θ_{RS}), move tetrahedral 8a iron ions to 16c sites to make a defective rock-salt phase (designated θ_{RS}) at fixed volume. Step 2: Expand the lattice to match the final $LiFe_3O_4$ lattice constant. Step 3: Insert lithium into vacant 16c sites from lithium metal to form $LiFe_3O_4$ (designated $Li\theta_{RS}$). All calculations are in a two formula unit cell.

The correlation plot in Fig. 6b shows the results. The structures where Fe^{2+} cations were maintained on 16c sites are shown in grey and those in which an alternate charge order was explored are in yellow. Across all the structures studied, the Madelung energy drives the final energy distribution. Similar correlations have been previously shown as the driving force for vacancy ordering on the 16d site in the maghemite (γ-Fe_2O_3) phase.[49] It can also be seen that the alternate charge order allowed for sampling of structures with lower Madelung energy, explaining how a lower final energy was achieved in the structure visualized in Fig. 7a.

In the two formula unit $LiFe_3O_4$ cell, we found that the lowest energy configuration exhibited antiferromagnetic (AFM) order (15 meV/atom more stable than a competing ferromagnetic order), in agreement with previous results.[31,95] A previous study based on a four formula unit cell also identified an antiferromagnetic phase as lowest in energy within that

constraint.[28] We note that the antiferromagnetic order found in those cases differs from the <111> AFM order in FeO, illustrated for reference in the SI, Fig. S4a. Specifically, for FeO, all Fe in a <111> plane exhibit parallel spin, while they are anti-parallel between <111> planes. For the two f.u. antiferromagnetic $LiFe_3O_4$ structure, the spin coupling is modulated through the 16c and 16d Wyckoff sites in Fd-3m, which cannot order in <111> planes due to symmetry. In the eight formula unit cell, ferromagnetic, ferrimagnetic, and antiferromagnetic orderings were tested for a sampling of ionic arrangements spanning the range shown in Fig. 6a. The lowest energy magnetic order was found to be ferrimagnetic in all of the eight formula unit cells tested. This particular structure could be visualized, starting from the corresponding ferrimagnetic order in the inverse spinel structure. The 8a irons shifted to 16c sites while maintaining spin down and the 16d irons maintained spin up. An example of this spin structure is shown in Fig. 7a. For comparison, the most stable spin structures found for the two formula unit cell is visualized in Fig. 7b.

As noted in Sect. 2.2, in terms of a Heisenberg local spin-spin coupling model for FeO, the second neatest neighbor, iron-iron interaction (J_2) dominated and determined the type-II antiferromagnetic order (along 111) for FeO (see also the SI, Fig. S4).[71] The J_2 interaction acts along the Cartesian directions in Fig. 7, linking iron cations through apical oxygens with an approximately 180° bond angle at the oxygen, as depicted in the figure. For a given ionic arrangement there is more than one way to maximize the second nearest neighbor interaction. But in particular, if the iron at the 16c sites have opposite spin to the iron on the 16d sites, the J_2 driven coupling is maximized. (The relationships between 16c and 16d and J_2 interaction is shown in Fig. S4a in a more simplified representation of the cell.) This explains why we found ferrimagnetic coupling to be the lowest magnetic order in the eight formula unit cell scheme that we used (eight spin down

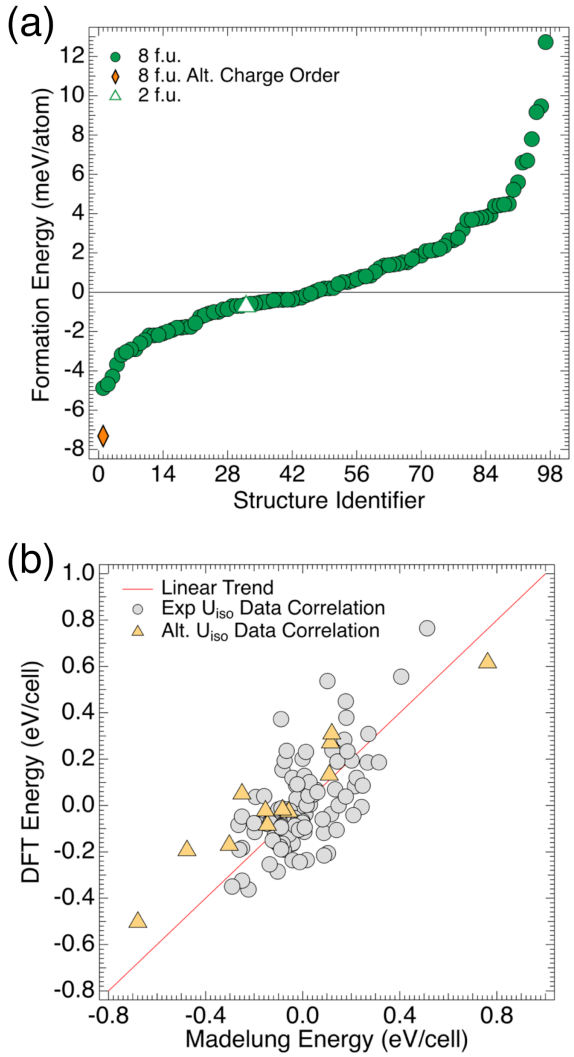

Figure 6. Stability of $LiFe_3O_4$ in the rock-salt-like structure relative to FeO and $LiFeO_2$. (a) Formation energy (green symbols) computed for the 97 symmetry distinct configurations of Li and Fe on the 16c site in the eight formula unit cell (circles) and for the one distinct configuration in the two formula unit cell (triangle). One alternate charge order was energetically competitive, shown in orange (diamond). (b) Correlation between the DFT energy of all 97 relaxed $LiFe_3O_4$ ionic arrangements and the Madelung energy of the same relaxed ionic structure, each computed relative to the average value (grey circles). Alternate possible charge orders, explored for a subset of the structures, are shown in orange (triangles).

iron on 16c versus 16 spin up iron on 16d). However, the antiferromagnetic two formula unit structure found previously[31,95] and confirmed here (Fig. 7b) also maximizes the J_2 coupling.

With reference to Fig. 6a, the formation energy found with the two formula unit cell was already slightly negative (about -1 meV/atom), indicating a stable phase, but not by a large enough margin to be regarded as robust. However, in the eight formula unit cell, the lowest energy configuration was lower than the one identified from the two formula unit cell, by about 7 meV/atom. As seen in Sect. 2.5, Fig. 3 and in Table S4, the corrected DFT+U results were quite accurate and systematic for the formation energies of FeO, $LiFeO_2$, Li_5FeO_4, and $LiFe_5O_4$, relative to metallic iron and lithium, and molecular oxygen under standard conditions. In particular, the FeO formation is overestimated by about 40 meV/atom while the three reference compounds containing lithium and iron together are within 10 meV/atom. With the FeO reference in particular being slightly over bound, our estimate for the stability of $LiFe_3O_4$ should be a lower bound. It should also be noted that in the stability calculation for $LiFe_3O_4$ relative to FeO and $LiFeO_2$, the iron and oxygen content are fixed, so the corrections that are significant for absolute formation energies drop out of the relative stability calculation. Finally, in DFT-based calculations, the relative energies are generally found to be much more accurate in practice. Taken together, our finding of relative stability for $LiFe_3O_4$ in the Li-Fe-O phase diagram is likely robust.

The larger unit cell has allowed for distributions of the ions that significantly better optimized the electrostatic energy. Specifically, in the two formula unit cell, the ions are constricted to charge ordering along the <100> direction. However, in the eight formula unit cell, there is no directional constriction for the charge distribution within the bounds of the cubic cell. The absence of a clearly imposed directional ordering for charge in the eight formula unit cell was further reflected in the result that many of the 97 symmetry unique ionic orders relaxed to P1, or were absent of symmetry.

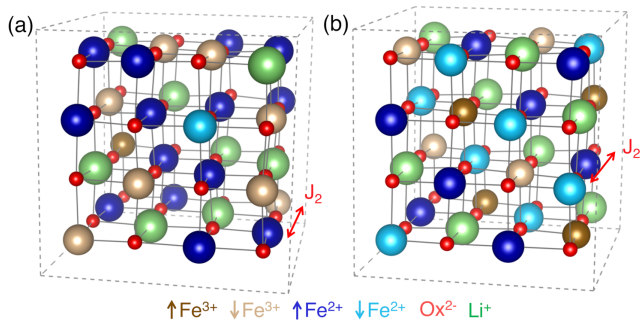

Figure 7. Low energy configurations of $LiFe_3O_4$ in the rock-salt-like structure. (a) Lowest energy configuration in the eight formula unit with Fe^{2+} on 16c sites. (b) Two formula unit cell relaxed structure represented in the eight formula unit cell. The origin is chosen midway between the cation and the anion along (111) so that all atoms shown are within the bounds of the unit cell shown by the dashed lines. An example of the second nearest neighbor spin-spin interaction between iron cations (J_2) is shown by the red arrow.

The calculations in the larger, eight formula unit cell also revealed that the distribution of formation energies (Fig. 6a) was essentially continuous as a function of lithium cation configuration. Thus, while the computed formation energy indicated a stable material at this composition, there was not a specific, well-defined phase found to associate with $LiFe_3O_4$.

The energies for the lowest ten configurations span about 20 meV/Li. While we have primarily focused on the zero temperature energy here, we have used the sampling of configurations in the eight formula unit cell to make an estimate of the contribution of Li-Fe configurational entropy.[74] For reference, the high temperature limit in the eight formula unit cell can capture 85.3% of the lattice gas analytical result. The computed result for the entropic contribution to the room temperature free energy was 19 meV/Li. This would correspond to an additional 2 meV/atom stabilization of $LiFe_3O_4$ at room temperature due to configurational entropy, relative to the FeO and $LiFeO_2$ endpoints.

3.3. Lithium Insertion into Spinel Fe_3O_4. Using the reference eight formula unit cell, the energy for lithium insertion to the 16c, 48f, and 8b, sites was compared, with full atomic and cell

shape relaxation in each case. In agreement with previous literature,[12] insertion to the 16c was lowest in energy, followed closely by the 48f site (0.05 eV/Li higher). The energy for the 8b site was considerably higher (2.4 eV/Li), as expected due to the repulsive near neighbor environment (Fig. 1b).

To investigate the dilute limit of isolated lithium insertion, a 16 formula unit cell was also constructed, with focus on the insertion to the 16c site. The computed energy gain, relative to metallic lithium, was -0.70 eV/Li. A similar result was found at a concentration of *x*=0.125 with the eight formula unit cell (-1.01 eV/Li). The lowest energy structures for *x*=0.0625 and 0.125 are shown in Fig. 8a and 8b respectively. The local, lithium centered motif clearly showed substantial displacement of one of the neighboring Fe^{3+} cations from its 8a site. The displacement was generally in the direction of the available empty 16c site. In the ideal *x*=0.0 lattice, the vacant 16c site was equidistant from two Fe_{8a} (1.81 Å from the 8a to the 16c site). In the relaxed magnetite structure, the angle defined by Fe_{8a}-$Vacant_{16c}$-Fe_{8a} deviated slightly from ideal (179.11°). After lithium insertion, the iron cation labeled 8a* in Fig. 8a had been displaced toward a vacant 16c site, moving 1.25 Å from its position in the *x*=0.0 lattice. The other proximal iron cation, 8a**, displaced by only 0.15 Å. However, the lithium inserted on the 16c site moved 0.59 Å from the high symmetry 16c site, off the high symmetry Fe_{8a}-$Vacant_{16c}$-Fe_{8a} line. The net result was an angle of 132.13° for Fe_{8a}-Li_{16c}-Fe_{8a} and the two corresponding cation distances were Li-Fe_{8a*} = 2.39 Å (8a*) and Li-Fe_{8a**} = 2.48 Å. With these structural changes, the distance between Fe_{8a*} and Fe_{8a**} had gone from 3.62 Å in the *x*=0.0 lattice to 4.50 Å in the *x*=0.0625 lattice. Note that in Figs. 8a and 8b, each of Fe_{8a**}, lithium, and Fe_{8a*} sit at a different depth along the axis perpendicular to the plane of the visualization.

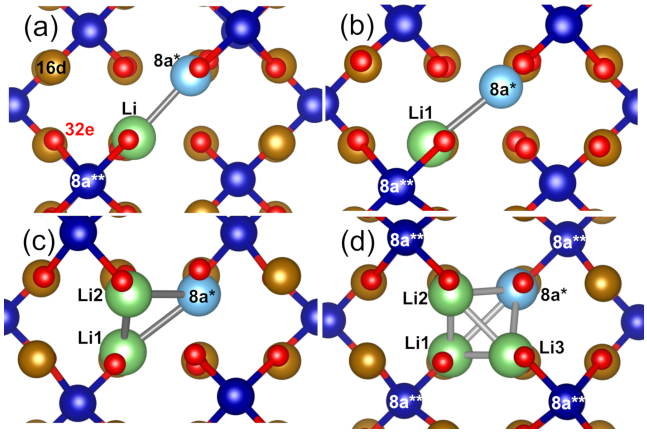

Figure 8. Lowest energy structures for Li insertion into 16c sites of spinel Fe_3O_4. (a) $Li_{0.0625}Fe_3O_4$, (b) $Li_{0.125}Fe_3O_4$, (c) $Li_{0.25}Fe_3O_4$, and (d) $Li_{0.375}Fe_3O_4$. Brown atoms are Fe_{16d}, red atoms are oxygen at 32e, dark blue atoms are Fe_{8a}, green atoms are lithium inserted at 16c sites, light blue atoms are Fe_{8a} that have been displaced due to proximal Li_{16c}. Projection along <100> in the cubic unit cell.

For *x*=0.125, there were differences in the details of the local motif around the inserted lithium. This was affected by restrictions of the eight formula unit cell, in part, since it does not allow for unique iron cations at the third neighbor shell, in contrast to what was allowed in the 16 f.u. cell. The first shell distances and angle were similar (Li-Fe_{8a*} = 2.45 Å, Li-Fe_{8a**} = 2.42 Å, Fe_{8a*}-Fe_{8a**} = 4.45 Å, lithium displaced from 16c by 0.52 Å, and Fe_{8a}-Li_{16c}-Fe_{8a} angle 132.09°). The nominal Fe_{8a*} and Fe_{8a**} displaced from the 8a positions in the *x*=0.0 structure by 0.79 Å and 0.40 Å respectively for *x*=0.125, a more symmetric distortion than found for *x*=0.0625. Finally, the magnitude of Fe_{8a} displacements dropped off substantially in the second Li-Fe_{8a} coordination shell, comprised of six atoms, namely to 0.10 Å for *x*=0.125 and 0.06 Å for *x*=0.0625 on average.

All symmetry distinct configurations for addition of two and three lithium atoms, *x*=0.25 and *x*=0.375, respectively, to 16c sites in the eight formula unit cell were investigated. Figures 8c and 8d illustrate the lowest energy structures found. The results clearly demonstrated clustering of the added lithium atoms in this regime. With reference to Fig. 1, each 8a site has four vacant 16c site nearest neighbors. As shown in Fig. 8b, the first inserted lithium, Li1, on one of the vacant

16c sites led to displacement of the proximal tetrahedral Fe_{8a*}, towards a second one of the vacant 16c sites. As noted above, this displacement cost substantial energy. There were two remaining empty 16c sites in the local motif seen in Fig. 8b. As illustrated in Fig. 8c, the lowest energy site found for addition of Li2 was adjacent to Li1, where the two lithium atoms could share the energy cost of the displacement of the Fe_{8a*}. The average energy gain was larger (-1.13 eV/Li).

A third added lithium, Li3, preferentially went onto the final vacant 16c site adjacent to Li1 and Li2 and the displaced Fe_{8a*} (Fig. 8d). This local motif resulted in even larger average energy gain (-1.30 eV/Li). The local Fe_{8a*} displaced further with each added lithium, approaching the 16c site (specifically 0.84 Å, 0.62 Å, and 0.34 Å away for x=0.125, 0.25, and 0.375, respectively). In the case of three inserted lithiums, their local motif including the displaced Fe_{8a} comprised a tetrahedron, centered on the original 8a site, with each atom near a neighboring 16c site, as shown in Fig. 8d. Surprisingly this tetrahedral motif had only a small impact on the adjacent Fe_{8a**} in Fig. 8d. The absolute value of the displacements of those Fe_{8a**} was on average 0.18 Å from the x=0.0 fully relaxed structure.

These results illustrate how the increasing concentrations of lithium cooperatively pushed the local Fe_{8a} iron into a 16c site. This cooperative force was maximized at x=0.375, as all the available local 16c sites in this tetrahedral motif had been exhausted. Furthermore, the cooperative displacement of all of the 8a iron cations in the structure to 16c sites previously hypothesized in the literature and discussed in the introduction, had not yet occurred.

The lowest energy motif based on insertion of an additional lithium into an eight formula unit cell, x=0.5, starting from spinel still showed clustering, but with four lithium atoms around two displaced iron cations from 8a sites. However, competing with this were x=0.5 configurations

with full conversion of all tetrahedral irons to 16c sites and lithium at 16c sites dispersed throughout the structure, which were found to be lower in energy than the structures based on clustering (as discussed in the next section). Thus, it was found that cluster motifs formed from the inserted lithium and displaced Fe_{8a} were energetically favored over lithium being distributed more uniformly throughout the cell, up to a concentration of x=0.375, or three Li^+ in an eight formula unit cell.

3.4. Lithium Insertion into Defective Rocksalt Fe_3O_4. Referring to Fig. 2, the relative stability of lithium intercalated magnetite should generally be determined relative to the corners of the Gibbs triangle consisting of FeO, Fe_3O_4 and $Li_2Fe_2O_4$. However, our calculations showed that $LiFe_3O_4$ was below the convex hull and that this composition of rock-salt-like structures was stable in the Li-Fe-O phase diagram. Therefore, to understand the stability and competition between the intercalated spinel structures discussed in Section 3.3 and the fully converted rock-salt-like

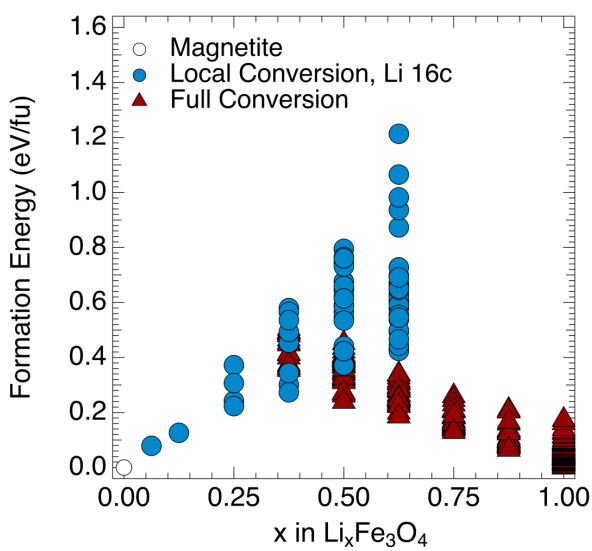

Figure 9. Convex-Hull for lithium insertion into Fe_3O_4 for $0 \leq x \leq 1$. All symmetry distinct configurations were sampled for insertion into the 16c site of the inverse spinel phase up to x=0.625, labeled local conversion (blue circles). Full Conversion corresponds to a defective rocksalt structure (red triangles). Starting from a complete sampling for x=1, selective sampling was done to probe competitive configurations shown here over the range x=0.375 to 0.875 as discussed in the text.

structures for 0.125 < x < 0.875, a one-dimensional convex hull has been computed with Fe_3O_4 and $LiFe_3O_4$ as the end points. In particular, as described in Sect. 2.3, a sequence of defective rocksalt structure for $Li_xFe_3O_4$ with 0.125 < x < 0.875 was sampled starting from a subset of the 97 configurations previously computed at x=1.0 and introducing lithium vacancies sequentially.

The comprehensive results for lithium insertion in the range $0 \leq x \leq 1$ are summarized in Fig. 9. From the lowest concentration probed here (x=0.0625), no insertion compound was found to be stable. As discussed above (Sect. 3.3), this traced back to the strong Coulomb repulsion between the inserted lithium and the iron cation on the 8a site. The energy cost to displace Fe_{8a} was simply too high. Even though the results for low concentration did show a stable local motif with up to three lithium atoms around a single displaced Fe_{8a} (Fig. 8d) in the spinel structure, this motif was not found to be stable against phase segregation to form the rocksalt-like phase and unlithiated magnetite. The results calculated for structures with lithium removed from $LiFe_3O_4$ are also shown in Fig. 9. More detail of the sampling is illustrated in the SI, Fig. S2. Starting with x=0.5, the lowest energy defective rock-salt structures were lower in energy than those based on insertion to the inverse spinel magnetite structure. In this sense, one could argue that the conversion to rock-salt occurs near x=0.5. However, these structures (0.5 < x < 0.875) were also found to be unstable against phase segregation to magnetite and the stable rock-salt end-point compound, $LiFe_3O_4$. Figure 9 shows that our DFT calculations predicted no stable range of range for lithium insertion. For 0 < x < 1, the calculations predicted two phase behavior.

3.5. Impact of Iron Vacancies on Lithium Insertion. The site preference for a nominally isolated iron vacancy was tested in an eight formula unit cell. In agreement with experiment,[45] an iron vacancy on the 16d site was found to be energetically preferred over a vacancy on the 8a site,

by 1.1 eV/vacancy. In the case of defective magnetite, $Fe_{2.875}O_4$, the charge distribution among the 15 occupied 16d sites was the expected ten Fe^{3+} and five Fe^{2+}, with the eight Fe^{3+} on the tetrahedral 8a sites unaffected by the presence of the 16d vacancy. Individual iron magnetic moments were largely unaffected, but the net magnetic moment was reduced to 3.70 μ_b per f.u. for $Fe_{2.875}O_4$. For maghemite, $Fe_{2.67}O_4$, all cation sites were Fe^{3+}, as expected and the net magnetic moment was further reduced to 3.29 μ_b per f.u., compared to the experimentally bulk value of 2.83 μ_b per f.u.[96–98]

In an iron deficient magnetite structure, lithium insertion to an iron vacancy on a 16d site competes with the interstitial sites previously examined for pristine magnetite (16c, 8b, or 48f). In $Fe_{2.875}O_4$ lithium insertion was most stable on the 16d iron vacancy defect, specifically by 38 meV/Li over insertion at a vacant 16c site. As visualized in Fig. 10a, all atoms in the lattice remained essentially undisturbed in the presence of the 16d lithium. Adding another lithium atom, it wafound that the lowest energy configuration was a split interstitial motif in which the two lithium cations shared the available 16d site (Fig. 10b). Alternative structures, in which the second lithium atom went to a more remote interstitial site resulted in the same type of local motif

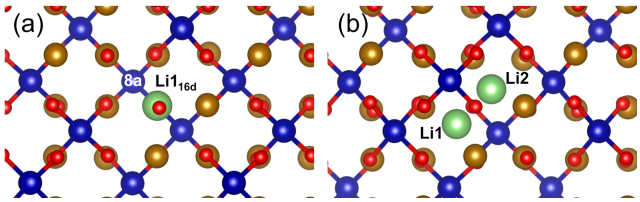

Figure 10. Lowest energy structures for lithium insertion into iron deficient magnetite to form $Li_xFe_{2.875}O_4$. (a) Lithium atom insertion to fill an iron vacancy on 16d (x=0.125). (b) Insertion of two lithium atoms to a single iron vacancy on a 16d site to form a split interstitial structure (x=0.25). Brown atoms are Fe_{16d}, red atoms are oxygen at 32e, dark blue atoms are Fe_{8a}, green atoms are lithium inserted at or near a 16d site. Projection along <100> in the cubic unit cell.

as illustrated in Fig. 8b, with the added cost of local displacement of the neighboring 8a site iron cation. They were therefore less stable than the split interstitial.

The stability of $Li_xFe_{2.875}O_4$ structures against phase segregation was tested by extending the analysis used for the ideal magnetite case. Focusing on the end point, $Li_{1.125}Fe_{2.875}O_4$, a physical set of configurations was developed as described in Sect. 2.3. Results for calculations done for the 16 identified configurations are shown in Fig. 11a and the lowest energy structure is visualized in the SI, Fig. S5. In addition to restrictions derived from the specific organization of iron and lithium cations on the 16c site, this search also excluded more extensive iron and lithium redistribution over the 16c + 16d sites. While the constrained search may not have revealed the most energetically favorable end-point, the calculated formation energy was still -5 meV/atom below the computed FeO to $\alpha-LiFeO_2$ tie line, similar to the $LiFe_3O_4$ stability of -7 meV/atom. Additionally, $Li_{1.125}Fe_{2.875}O_4$ is less than 1 meV/atom above the predicted $LiFe_3O_4$ + $LiFeO_2$ tie line. Using it as an end point to form a convex hull to examine lithium insertion into $Fe_{2.875}O_4$, the formation energies shown in Fig. 11a indicate that a single lithium atom on the available vacancy site was a stable intercalate. However, lithium insertion on the 16c site was unstable and the x=0.25 split interstitial motif was also unstable against phase segregation. This further exemplifies the strong Coulomb repulsion between the 16c site and the 8a site occupied by iron that destabilized insertion into pristine spinel.

The natural, high concentration limit of 16d iron vacancies in magnetite is x=0.33, corresponding formally to all iron sites being Fe^{3+} and exemplified by maghemite, γ-$Fe_{2.67}O_4$. Following the same trend as in defective magnetite, $Li_xFe_{2.875}O_4$, lithium insertion onto 16d sites up to the concentration of the vacancies resulted in stable intercalated structures, as illustrated in

Fig. 11b. Similar to intercalation of lithium to an isolated vacancy, there were no structural rearrangements of the parent γ-$Fe_{2.67}O_4$. Analogous to $Fe_{2.875}O_4$ and Fe_3O_4, lithiation at a 16c site in γ-$Fe_{2.67}O_4$ was unstable due to Coulombic interactions between the Li_{16c} and Fe_{8a}. The computed formation energy is shown in Fig. 11b and it is above the hull.

The supercell for γ-$Fe_{2.67}O_4$ with 24 formula units was too large either to enumerate all possible orderings of lithium and iron cations on the 16c sites as was done for $LiFe_3O_4$ or to sample in a constrained way, as was done for $Li_{1.125}Fe_{2.875}O_4$. As such, concentrations between $0.33 < x < 1.33$ were not sampled. However, due to the knowledge gained from the $Li_xFe_3O_4$ and $Li_xFe_{2.875}O_4$ structures, insertion of lithium past the concentration of vacancies will likely result in Coulombic repulsions and instability with respect to the rocksalt end point, $Li_{1.33}Fe_{2.67}O_4$. Due to computational cost, only one structure for the $Li_{1.33}Fe_{2.67}O_4$ end point was calculated. This structure was characterized by maintaining the vacancy order on the 16d site according to $P4_12_12$ order found to be most stable by Grau-Crespo, *et al*.[49] The lithium and iron cations on the 16c site were set as visualized in the SI, Fig. S5. The $Li_{1.33}Fe_{2.67}O_4$ phase calculated was found to be 8 meV/atom above the tie line to phase segregation to FeO to α-$LiFeO_2$ and 12 meV/atom above the $LiFe_3O_4$ to $LiFeO_2$ tie line. With the large size of the entirely unexplored configurational space as well as the small energetic distance to the tie line, with further optimization, likely a lower energy structure could be found.

3.7. Open Circuit Potential. We now consider the implications for the open circuit potential of our computed stability results for lithium insertion. Lithium insertion up to the concentration of iron vacancies on the 16d site was found to be stable. However, beyond this point, the calculations predicted two-phases in equilibrium. The respective end points depend on iron vacancy

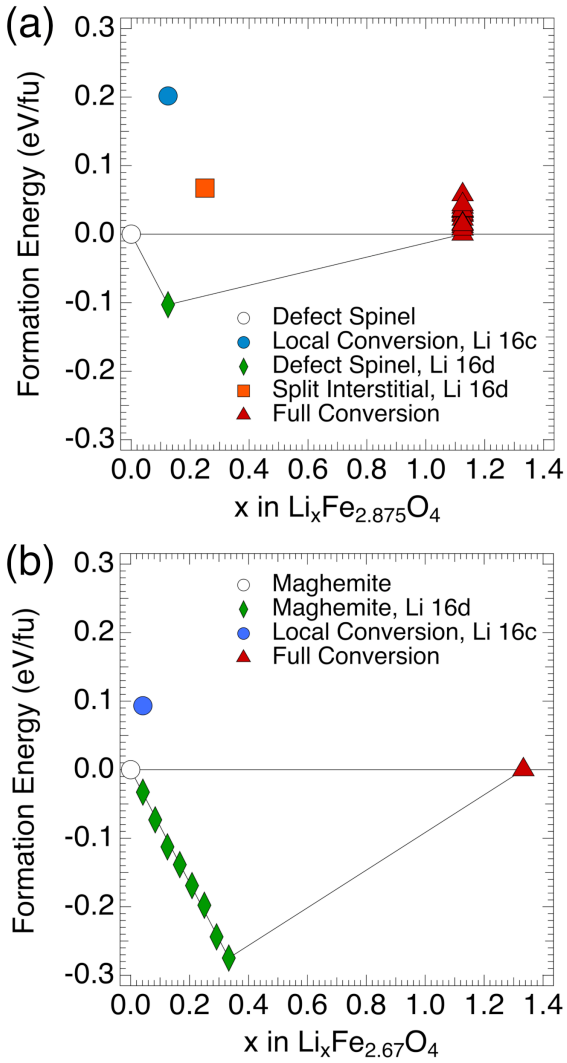

Figure 11. Convex-Hull for lithium insertion into iron deficient magnetite. (a) One iron vacancy per eight formula units: $Fe_{2.875}O_4$. (b) Maghemite formed as an ordered structure of eight iron vacancies in a 24 formula unit cell: $Fe_{2.67}O_4$.

concentration, being Fe_3O_4 and $LiFe_3O_4$, $Li_{0.125}Fe_{2.875}O_4$ and $Li_{1.125}Fe_{2.875}O_4$, and $Li_{0.33}Fe_{2.67}O_4$ and $Li_{1.33}Fe_{2.67}O_4$, in the cases studied here. The DFT+U predicted voltages of the two-phase equilibria for lithium insertion into Fe_3O_4, $Fe_{2.875}O_4$, and $Fe_{2.67}O_4$ are shown in Fig. 4b, in overlays on the measured data.

The convex hull stability analysis predicted that lithium insertion into magnetite resulted in phase segregate into Fe_3O_4 and $LiFe_3O_4$. However, an analysis of the predicted voltages for the

lithium clustering motifs in Fig. 8 gives insight into whether these motifs could occur in a metastable structure. For the *x*=0.375, the calculated energy for the three lithium cluster motif depicted in Fig. 8d predicted a voltage of 1.30 V. Of course, this was smaller than the predicted voltage for two phase formation (~ 2 V). But, the experimentally observed voltage at *x*=0.375 was ~2.6 V. Similarly, for *x*=0.125, the predicted voltage for the lithium cluster motif was 1.01 V, while the experimentally observed voltage was ~2.8 V. Finally, the *x*=0.25 split interstitial in Fig. 10 b occurred at a DFT predicted potential of 0.80 V, while the experimental voltage was ~2.7 V. Due to such a large discrepancy between the predicted voltage for the local lithium clustering motifs and the experimentally observed voltages in the low concentration range, it is unlikely that these structures contribute to the experimentally observed reversible potential as metastable local motifs.

From the experimental data in Fig. 4b, it was observed that the reversible potential for lithiation of 8-9 nm Fe_3O_4 nanoparticles initiated with an intercalation regime from 2.8-1.8 V, followed by a two-phase voltage plateau at around 1.8 V. When iron vacancies occur in the material, as in the case of $Fe_{2.875}O_4$ and $Fe_{2.67}O_4$, lithiation into these vacancies resulted in stable intercalates, in particular energetically favorable against phase segregation. The predicted voltages for iron vacancy filling by lithium were 2.87-3.01 V, consistent with the experimental voltage range for early lithiation into the 8-9 nm particles reported in Fig. 4b. Further lithiation past the concentration of 16d iron vacancies, resulted in phase segregation at a DFT+U predicted voltage of 1.89-2.02 V, consistent with the first experimental voltage plateau in Fig. 4b.

4. CONCLUSIONS

The results of the stability analysis for lithium insertion into Fe_3O_4, $Fe_{2.875}O_4$, and γ-$Fe_{2.67}O_4$ are summarized in Fig. 12, a zoom-in on the pertinent region of the Li-Fe-O ternary phase diagram from Fig. 2. Robustly stable structures are shown in green, unstable in red, and marginally stable or not sufficiently sampled are in white with green or black outline, respectively. Our calculations have probed the stability of lithium in three different scenarios. First, in the region highlighted in green, the basic structure is that of inverse spinel. Our results indicate stable phases formed when lithium substitutes for iron on the octahedral 16d sites. Second, along the tie line between FeO and $LiFeO_2$, the basic structure is rock-salt. Our calculations predict stable formation of $LiFe_3O_4$ specifically. Third, we explored lithium insertion into the material in the region that connects the spinel region and the rock-salt tie-line where we found no range of stable intercalation by lithium, just two phase behavior.

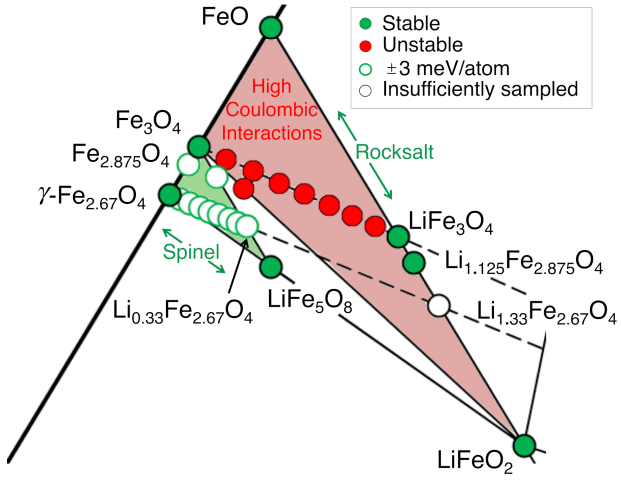

Figure 12. Zoom in on the Li-Fe-O ternary phase diagram assessing the computed stability of compounds formed by lithiation of magnetite. Results shown starting from stoichiometric Fe_3O_4 and two representative iron deficient structures, $Fe_{2.875}O_4$, and $Fe_{2.67}O_4$. Green solid circles indicate clearly stable phases. Red solid circles indicate clearly unstable phases. Cases where the formation energy was close to zero are shown with open green circles. Red shaded region highlights the area where phase segregation is clearly driven by Coulomb repulsion. Green shaded region highlights the area where lithium can intercalate onto a 16d cation vacancy sites.

Magnetite is known to have iron vacancies on the 16d sites. These compositions occur along the tie line in Fig. 12 connecting Fe_3O_4 to γ-$Fe_{2.67}O_4$, corresponding to the highest concentration of vacancies observed while maintaining the spinel structure (*x*=0.33, maghemite). The observed $LiFe_5O_8$ compound is also a spinel structure with one quarter of the 16d site iron atoms replaced by lithium. Our observation that phases formed by lithium insertion to fill iron vacancies on 16d sites ($(Fe)_{8a}[Li_{\delta}Fe_{2-\delta}]_{16d}[O_4]_{32e}$) were stable is fully consistent with this picture. The significant finding was that the voltage predicted for insertion to the vacancies matches very well to the experimentally measured voltages in the low lithium concentration range. However, this appealing and simple picture does not explain the observed continuous variation in open circuit potential typically associated with intercalation behavior in Fig. 4b up to *x* ~ 0.8. This indicates that there are likely other mechanisms by which intercalation proceeds in the nanoparticles. Further investigation into the chemistry and termination of particle surfaces, the interaction between pristine and iron defective regions of the particles, iron extrusion, and other side reactions are all possible considerations.

Along the line connecting FeO to $LiFeO_2$, a series of defective rock-salt structures with saturated cation occupancy but variable concentration of lithium versus iron can be considered ($Li_xFe_{1-x}O$, $0 < x < 0.5$). Across this range, the nominal oxidation state of the iron varies from Fe^{2+} to Fe^{3+}. We specifically considered the cases $LiFe_3O_4$, $Li_{1.125}Fe_{2.875}O_4$, and $Li_{1.33}Fe_{2.67}O_4$. As for the case of magnetite, the mixture of iron valences in these compounds presents significant extra complexity related to ordering of the charge in a local picture and the corresponding Jahn-Teller distortions and orbital selection associated with the Fe^{2+}. We calculated fully relaxed structures for an extensive sampling of Li-Fe configurations in the specific case of $LiFe_3O_4$ in an eight formula

unit cell. We found that the distribution of lithium cations for each configuration drove the charge ordering among the iron cations to a large extent, with an energy scale essentially an order of magnitude larger than that found for the higher symmetry pure magnetite case. In the scope of those configurations, we found many configurations that were energetically stable with respect to phase segregation to FeO and $LiFeO_2$. Naturally, we could not exhaustively search for all possible combinations of charge ordering and orbital ordering even within the eight formula cell, not to mention alternative cell sizes or symmetries. However, identification of even lower energy configurations would only strengthen our main conclusion, namely the relative stability of $LiFe_3O_4$.

Our calculations for other compositions along the FeO to $LiFeO_2$ tie line could not be as detailed due to the larger number of configurations involved. Nonetheless, they point to the idea that along this line in the phase diagram in Fig. 12, there could likely be a range of Li-Fe compositions that could be easily realized in experiment. Observations of rock-salt structures for compounds with nominal concentration in this range have been very common in the literature, as discussed in the introduction. However, the specific organization of lithium in the structure typically could not be determined. This may be in part due to difficulty in detecting the contribution of the light lithium atoms in the diffraction studies. However, it is also consistent with our observation of an essentially continuous distribution of energies for different Li-Fe configurations for the $LiFe_3O_4$ case. For any practical temperature at which cation mobility freezes out in sample preparation, it would be unlikely to expect strong, long-range order among the lithium and iron cations.

For lithium insertion into magnetite (or iron deficient magnetite beyond the vacancy concentration), our calculations predict phase segregation. Focusing on the tie line between Fe_3O_4

and $LiFe_3O_4$, the one dimensional convex hull in Fig. 9 illustrates this clearly. Our sampling of charge and orbital order may not have revealed the lowest energy structures possible for each composition. However, in the low lithium concentration region, the lithium cluster motifs identified here will only locally disrupt the charge and orbital ordering of the parent magnetite. Therefore, it is likely that further consideration of such ordering will only further stabilize the magnetite end point. Also, the overall energy scale identified for charge and orbital ordering (and connected to the Verwey transition temperature) is small compared to the energy scale seen in the convex hull. Similarly, the energy cost to introduce a lithium vacancy into $LiFe_3O_4$ is also higher than both that for orbital and charge ordering. While configurational entropy effects, e.g., at room temperature, will generally stabilize vacancies over a relatively low concentration range, they will not be large enough to affect the results for the concentrations shown in Fig. 9. Further, the configurational entropy calculated for the full set of 97 $LiFe_3O_4$ structures (2 meV/atom) is commensurate with the configurational entropy of the Verwey transition[99] at the x=0.0 end point of the convex hull. These arguments suggest that the prediction of phase segregation is robust. Finally, the predicted open circuit potential associated with the phase segregation agrees well with the voltage measured on the plateau region.

In summary, the new measurements and the analysis based on computations presented here provide a picture for the thermodynamic stability of compounds formed from magnetite and iron deficient magnetite upon lithium insertion. Insertion to fill iron vacancies is responsible for relatively high open circuit voltages at low lithium concentration. Phase segregation with a rock-salt-like end point explains the voltage plateau. This thermodynamic picture can serve as the basic

starting point for future understanding of kinetic effects, side reactions and other effects in consideration of the lithiation of magnetite nanoparticles.

ASSOCIATED CONTENT

Supporting Information

The Supporting Information is available free of charge on the ACS Publications website at DOI: TBD.

Supporting discussion, tables and figure, and structure information: (1) Fe_3O_4 charge and orbital ordering tests; (2) $LiFe_3O_4$ charge ordering tests; (3) Li-Fe-O ternary phase diagram; (4) Tables S1-S4 and Figures S1-S5; and (5) Lowest energy $LiFe_3O_4$ structure in CIF format.

AUTHOR INFORMATION

Corresponding Authors

*E-mail: mhyberts@bnl.gov.

ORCID

Christianna N Lininger: 0000-0001-7005-6913

Kenneth J. Takeuchi: 0000-0001-8129-444X

Amy C. Marschilok: 0000-0001-9174-0474

Esther S. Takeuchi: 0000-0001-8518-1047

Alan C. West: 0000-0002-3524-3040

Mark S. Hybertsen: 0000-0003-3596-9754

ACKNOWLEDGMENTS

The authors thank Yan Li for providing unpublished details of her DFT-based computations that contributed to Ref. 31. C. N. L. acknowledges the support of the National Science Foundation Graduate Research Fellowship under Grant No. 1644869. This work was supported as part of the Center for Mesoscale Transport Properties, an Energy Frontier Research Center supported by the U.S. Department of Energy (DOE), Office of Science, Basic Energy Sciences, under Award DE-SC0012673. A portion of this work was performed using facilities in the Center for Functional Nanomaterials, which is a U.S. DOE Office of Science User Facility, and the Scientific Data and Computing Center, a component of the Computational Science Initiative, at Brookhaven National Laboratory under Contract No. DE-SC0012704. This work also used Columbia University's Shared Research Computing Facility project, which is supported by NIH Research Facility Improvement Grant 1G20RR030893-01, and associated funds from the New York State Empire State Development, Division of Science Technology and Innovation (NYSTAR) Contract C090171, both awarded April 15, 2010. This work also used the Extreme Science and Engineering Discovery Environment (XSEDE), which is supported by National Science Foundation grant number ACI-1548562. XSEDE Stampede and Stampede2 were used through allocation TG-DMR160174 and TG-DMR160128. Any opinions, findings, and conclusions or recommendations expressed in this material are those of the authors and do not necessarily reflect the views of the National Science Foundation.

REFERENCES

(1) Thackeray, M. M. Spinel Electrodes for Lithium Batteries. *J. Am. Ceram. Soc.* 1999, *82* (12), 3347–3354.

(2) Poizot, P.; Laruelle, S.; Grugeon, S.; Dupont, L.; Tarascon, J. M. Nano-Sized Transition-Metal Oxides as Negative-Electrode Materials for Lithium-Ion Batteries. *Nature* 2000, *407* (6803), 496–499.

(3) Whittingham, M. S. Lithium Batteries and Cathode Materials. *Chem. Rev.* 2004, *104* (10), 4271–4301.

(4) Cabana, J.; Monconduit, L.; Larcher, D.; Palacín, M. R.; Palacin, M. R. Beyond Intercalation-Based Li-Ion Batteries: The State of the Art and Challenges of Electrode Materials Reacting through Conversion Reactions. *Adv. Mater.* 2010, *22* (35), 170–192.

(5) Abraham, A.; Housel, L. M.; Lininger, C. N.; Bock, D. C.; Jou, J.; Wang, F.; West, A. C.; Marschilok, A. C.; Takeuchi, K. J.; Takeuchi, E. S. Investigating the Complex Chemistry of Functional Energy Storage Systems: The Need for an Integrative, Multiscale (Molecular to Mesoscale) Perspective. *ACS Cent. Sci.* 2016, *2* (6), 380–387.

(6) Godshall, N. A.; Raistrick, I. D.; Huggins, R. A. Thermodynamic Investigations of Ternary Lithium-Transition Metal-Oxygen Cathode Materials. *Mater. Res. Bull.* 1980, *15* (5), 561–570.

(7) Thackeray, M. M.; David, W. I. F.; Goodenough, J. B. Structural Characterization of the Lithiated Iron Oxides LixFe304 AND LixFe203 (0<x<2). *Mater. Res. Bull.* 1982, *17*, 785–793.

(8) Thackeray, M. M.; David, W. I. F.; Goodenough, J. B. High-Temperature Lithiation of α-Fe203: A Mechanistic Study. *J. Solid State Chem.* 1984, *55* (3), 280–286.

(9) Chen, C. J.; Greenblatt, M.; Waszczak, J. V. Lithium Insertion Compounds of LiFe5O8, Li2FeMn3O8, and Li2ZnMn3O8. *J. Solid State Chem.* 1986, *64* (3), 240–248.

(10) Chen, C. J.; Greenblatt, M.; Waszczak, J. V. Lithium Insertion into Spinel Ferrites. *Solid State Ionics* 1986, *18* (Part 2), 838–846.

(11) de Picciotto, L. A.; Thackeray, M. M. Lithium Insertion into the Spinel LiFe5O8. *Mater. Res. Bull.* 1986, *21* (5), 583–592.

(12) Islam, M. S.; Catlow, C. R. A. Lithium Insertion into Fe3O4. *J. Solid State Chem.* 1988, *77* (1), 180–189.

(13) Pernet, M.; Strobel, P.; Bonnet, B.; Bordet, P.; Chabre, Y. Structural and Electrochemical Study of Lithium Insertion into γ-Fe2O3. *Solid State Ionics* 1993, *66* (3–4), 259–265.

(14) Ito, S.; Nakaoka, K.; Kawamura, M.; Ui, K.; Fujimoto, K.; Koura, N.; Kawamura, A.; Ui, K.; Fujimoto, K.; Koura, N. Lithium Battery Having a Large Capacity Using Fe3O4 as a Cathode Material. *J. Power Sources* 2005, *146* (1–2), 319–322.

(15) Kanzaki, S.; Inada, T.; Matsumura, T.; Sonoyama, N.; Yamada, A.; Takano, M.; Kanno, R. Nano-Sized γ-Fe2O3 as Lithium Battery Cathode. *J. Power Sources* 2005, *146* (1), 323–326.

(16) Taberna, P. L.; Mitra, S.; Poizot, P.; Simon, P.; Tarascon, J.-M. High Rate Capabilities Fe3O4-Based Cu Nano-Architectured Electrodes for Lithium-Ion Battery Applications. *Nat. Mater.* 2006, *5* (7), 567–573.

(17) Kanzaki, S.; Yamada, A.; Kanno, R. Effect of Chemical Oxidation for Nano-Size Gamma-Fe2O3 as Lithium Battery Cathode. *J. Power Sources* 2007, *165* (1), 403–407.

(18) Zhang, W. M.; Wu, X. L.; Hu, J. S.; Guo, Y. G.; Wan, L. J. Carbon Coated Fe3O4 Nanospindles as a Superior Anode Material for Lithium-Ion Batteries. *Adv. Funct. Mater.*

2008, *18* (24), 3941–3946.
(19) Zhu, S.; Marschilok, A. C.; Takeuchi, E. S.; Takeuchi, K. J. Crystallite Size Control and Resulting Electrochemistry of Magnetite, Fe3O4. *Electrochem. Solid-State Lett.* 2009, *12* (4), A91–A94.
(20) Komaba, S.; Mikumo, T.; Yabuuchi, N.; Ogata, A.; Yoshida, H.; Yamada, Y. Electrochemical Insertion of Li and Na Ions into Nanocrystalline Fe3O4 and α-Fe2O3 for Rechargeable Batteries. *J. Electrochem. Soc.* 2010, *157* (1), A60–A65.
(21) Hirayama, M.; Tomita, H.; Kubota, K.; Kanno, R. Structure and Electrode Reactions of Layered Rocksalt LiFeO2 Nanoparticles for Lithium Battery Cathode. *J. Power Sources* 2011, *196* (16), 6809–6814.
(22) Bock, D. C.; Pelliccione, C. J.; Zhang, W.; Wang, J.; Knehr, K. W.; Wang, J.; Wang, F.; West, A. C.; Marschilok, A. C.; Takeuchi, K. J.; et al. Dispersion of Nanocrystalline Fe3O4 within Composite Electrodes: Insights on Battery-Related Electrochemistry. *ACS Appl. Mater. Interfaces* 2016, *8* (18), 11418–11430.
(23) Bruck, A. M.; Cama, C. A.; Gannett, C. N.; Marschilok, A. C.; Takeuchi, E. S.; Takeuchi, K. J. Nanocrystalline Iron Oxide Based Electroactive Materials in Lithium Ion Batteries: The Critical Role of Crystallite Size, Morphology, and Electrode Heterostructure on Battery Relevant Electrochemistry. *Inorg. Chem. Front.* 2016, *3* (1), 26–40.
(24) Bock, D. C.; Pelliccione, C. J.; Zhang, W.; Timoshenko, J.; Knehr, K. W.; West, A. C.; Wang, F.; Li, Y.; Frenkel, A. I.; Takeuchi, E. S.; et al. Size Dependent Behavior of Fe3O4 Crystals during Electrochemical (de)Lithiation: An in Situ X-Ray Diffraction, Ex Situ X-Ray Absorption Spectroscopy, Transmission Electron Microscopy and Theoretical Investigation. *Phys. Chem. Chem. Phys.* 2017, *19* (31), 20867–20880.
(25) Yamauchi, S.; Hibino, M.; Yao, T. Structure Change Analysis in γ-Fe2O3/Carbon Composite in the Process of Electrochemical Lithium Insertion. *Solid State Ionics* 2011, *191* (1), 45–48.
(26) Park, S.; Matsui, T.; Takai, S.; Yao, T. Crystal Structure Analysis of γ-Fe2O3 with Chemical Lithium Insertion. *Solid State Ionics* 2014, *255*, 50–55.
(27) Knehr, K. W.; Brady, N. W.; Cama, C. A.; Bock, D. C.; Lin, Z.; Lininger, C. N.; Marschilok, A. C.; Takeuchi, K. J.; Takeuchi, E. S.; West, A. C. Modeling the Mesoscale Transport of Lithium-Magnetite Electrodes Using Insight from Discharge and Voltage Recovery Experiments. *J. Electrochem. Soc.* 2015, *162* (14), A2817–A2826.
(28) He, K.; Zhang, S.; Li, J.; Yu, X.; Meng, Q.; Zhu, Y. Y.; Hu, E.; Sun, K.; Yun, H.; Yang, X.-Q.; et al. Visualizing Non-Equilibrium Lithiation of Spinel Oxide via in Situ Transmission Electron Microscopy. *Nat. Commun.* 2016, *7* (May), 11441.1-11441.9.
(29) Brady, N. W.; Knehr, K. W.; Cama, C. A.; Lininger, C. N.; Lin, Z.; Marschilok, A. C.; Takeuchi, K. J.; Takeuchi, E. S.; West, A. C. Galvanostatic Interruption of Lithium Insertion into Magnetite: Evidence of Surface Layer Formation. *J. Power Sources* 2016, *321*, 106–111.
(30) Menard, M. C.; Takeuchi, K. J.; Marschilok, A. C.; Takeuchi, E. S. Electrochemical Discharge of Nanocrystalline Magnetite: Structure Analysis Using X-Ray Diffraction and X-Ray Absorption Spectroscopy. *Phys. Chem. Chem. Phys.* 2013, *15* (42), 18539–18548.
(31) Zhang, W.; Bock, D. C.; Pelliccione, C. J.; Li, Y.; Wu, L.; Zhu, Y.; Marschilok, A. C.; Takeuchi, E. S.; Takeuchi, K. J.; Wang, F. Insights into Ionic Transport and Structural Changes in Magnetite during Multiple-Electron Transfer Reactions. *Adv. Energy Mater.* 2016, *6* (10), 1502471.1-1502471.11.

(32) Mitra, S.; Poizot, P.; Finke, A.; Tarascon, J.-M. Growth and Electrochemical Characterization versus Lithium of Fe3O4 Electrodes Made by Electrodeposition. *Adv. Funct. Mater.* 2006, *16* (17), 2281–2287.
(33) Walz, F. The Verwey Transition - a Topical Review. *J. Phys. Condens. Matter* 2002, *14* (12), R285–R340.
(34) Senn, M. S.; Wright, J. P.; Attfield, J. P. Charge Order and Three-Site Distortions in the Verwey Structure of Magnetite. *Nature* 2011, *481* (7380), 173–176.
(35) Senn, M. S.; Loa, I.; Wright, J. P.; Attfield, J. P. Electronic Orders in the Verwey Structure of Magnetite. *Phys. Rev. B* 2012, *85* (12), 125119.1-125119.5.
(36) Anderson, P. W. Ordering and Antiferromagnetism in Ferrites. *Phys. Rev.* 1956, *102* (4), 1008–1013.
(37) Wright, J. P.; Attfield, J. P.; Radaelli, P. G. Charge Ordered Structure of Magnetite Fe3O4 below the Verwey Transition. *Phys. Rev. B* 2002, *66* (21), 214422.1-214422.15.
(38) Jeng, H.-T.; Guo, G. Y.; Huang, D. J. Charge-Orbital Ordering in Low-Temperature Structures of Magnetite: GGA+U Investigations. *Phys. Rev. B* 2006, *74* (19), 195115.1-195115.10.
(39) Zhou, F.; Ceder, G. First-Principles Determination of Charge and Orbital Interactions in Fe3O4. *Phys. Rev. B - Condens. Matter Mater. Phys.* 2010, *81* (20), 3–8.
(40) Jain, A.; Ong, S. P.; Hautier, G.; Chen, W.; Richards, W. D.; Dacek, S.; Cholia, S.; Gunter, D.; Skinner, D.; Ceder, G.; et al. Commentary: The Materials Project: A Materials Genome Approach to Accelerating Materials Innovation. *APL Mater.* 2013, *1* (1), 11002.1-11002.11.
(41) Braun, P. B. A Superstructure in Spinels. *Nature* 1952, *170* (4339), 1123.
(42) Thackeray, M. M.; Depicciotto, L. A.; Dekock, A.; Johnson, P. J.; Nicholas, V. A.; Adendorff, K. T.; de Picciotto, L. A.; de Kock, A.; Johnson, P. J.; Nicholas, V. A.; et al. Spinel Electrodes for Lithium Batteries - A Review. *J. Power Sources* 1987, *21* (1), 1–8.
(43) Fontcuberta, J.; Rodríguez, J.; Pernet, M.; Longworth, G.; Goodenough, J. B. Structural and Magnetic Characterization of the Lithiated Iron Oxide Li x Fe 3 O 4. *J. Appl. Phys.* 1986, *59* (6), 1918–1926.
(44) Knehr, K. W.; Cama, C. A.; Brady, N. W.; Marschilok, A. C.; Takeuchi, K. J.; Takeuchi, E. S.; West, A. C. Simulations of Lithium-Magnetite Electrodes Incorporating Phase Change. *Electrochim. Acta* 2017, *238*, 384–396.
(45) Daniels, J. M.; Rosencwaig, a. Mössbauer Spectroscopy of Stoichiometric and Non-Stoichiometric Magnetite. *J. Phys. Chem. Solids* 1969, *30* (6), 1561–1571.
(46) Gallagher, K. J.; Feitknecht, W.; Mannweiler, U. Mechanism of Oxidation of Magnetite to G-Fe2O3. *Nature* 1968, *217* (5134), 1118–1121.
(47) Shmakov, A. N.; Kryukova, G. N.; Tsybulya, S. V; Chuvilin, A. L.; Solovyeva, L. P. Vacancy Ordering in γ-Fe2O3: Synchrotron X-Ray Powder Diffraction and High-Resolution Electron Microscopy Studies. *J. Appl. Crystallogr.* 1995, *28* (2), 141–145.
(48) Jørgensen, J.-E.; Mosegaard, L.; Thomsen, L. E.; Jensen, T. R.; Hanson, J. C. Formation of G-Fe2O3 Nanoparticles and Vacancy Ordering: An in Situ X-Ray Powder Diffraction Study. *J. Solid State Chem.* 2007, *180* (1), 180–185.
(49) Grau-Crespo, R.; Al-Baitai, A. Y.; Saadoune, I.; De Leeuw, N. H. Vacancy Ordering and Electronic Structure of γ - Fe2O3 (Maghemite): A Theoretical Investigation. *J. Phys. Condens. Matter* 2010, *22* (25), 255401.1-255401.7.

(50) Hibino, M.; Terashima, J.; Yao, T. Reversible and Rapid Discharge–Charge Performance of γ–Fe2O3 Prepared by Aqueous Solution Method as the Cathode for Lithium-Ion Battery. *J. Electrochem. Soc.* 2007, *154* (12), A1107–A1111.
(51) Park, S.; Oda, M.; Yao, T. Relaxation Structure Analysis of Li Inserted γ-Fe2O3. *Solid State Ionics* 2011, *203* (1), 29–32.
(52) Frison, R.; Cernuto, G.; Cervellino, A.; Zaharko, O.; Colonna, G. M.; Guagliardi, A.; Masciocchi, N. Magnetite-Maghemite Nanoparticles in the 5-15 Nm Range: Correlating the Core-Shell Composition and the Surface Structure to the Magnetic Properties. A Total Scattering Study. *Chem. Mater.* 2013, *25* (23), 4820–4827.
(53) Zhu, S.; Marschilok, A. C.; Takeuchi, E. S.; Yee, G. T.; Wang, G.; Takeuchi, K. J. Nanocrystalline Magnetite: Synthetic Crystallite Size Control and Resulting Magnetic and Electrochemical Properties. *J. Electrochem. Soc.* 2010, *157* (11), A1158–A1163.
(54) Kresse, G.; Furthmüller, J. Efficient Iterative Schemes for Ab Initio Total-Energy Calculations Using a Plane-Wave Basis Set. *Phys. Rev. B* 1996, *54* (16), 11169–11186.
(55) Kresse, G.; Joubert, D. From Ultrasoft Pseudopotentials to the Projector Augmented-Wave Method. *Phys. Rev. B* 1999, *59* (3), 1758–1775.
(56) Blöchl, P. E. Projector Augmented-Wave Method. *Phys. Rev. B* 1994, *50* (24), 17953–17979.
(57) Perdew, J. P.; Burke, K.; Ernzerhof, M. Generalized Gradient Approximation Made Simple. *Phys. Rev. Lett.* 1996, *77* (18), 3865–3868.
(58) Anisimov, V. I.; Zaanen, J.; Andersen, O. K. Band Theory and Mott Insulators: Hubbard U Instead of Stoner I. *Phys. Rev. B* 1991, *44* (3), 943–954.
(59) Anisimov, V. I.; Aryasetiawan, F.; Lichtenstein, A. I. First-Principles Calculations of the Electronic Structure and Spectra of Strongly Correlated Systems: The LDA + U Method. *J. Phys. Condens. Matter* 1997, *9* (4), 767–808.
(60) Dudarev, S. L.; Savrasov, S. Y.; Humphreys, C. J.; Sutton, a. P.; Botton, G. A.; Savrasov, S. Y.; Humphreys, C. J.; Sutton, a. P. Electron-Energy-Loss Spectra and the Structural Stability of Nickel Oxide: An LSDA+U Study. *Phys. Rev. B* 1998, *57* (3), 1505–1509.
(61) Methfessel, M.; Paxton, A. T. High-Precision Sampling for Brillouin-Zone Integration in Metals. *Phys. Rev. B* 1989, *40* (6), 3616–3621.
(62) Meredig, B.; Thompson, A.; Hansen, H. A.; Wolverton, C.; van de Walle, A. Method for Locating Low-Energy Solutions within DFT+U. *Phys. Rev. B* 2010, *82* (19), 195128.1-195128.5.
(63) Santos-Carballal, D.; Roldan, A.; Grau-Crespo, R.; de Leeuw, N. H. A DFT Study of the Structures, Stabilities and Redox Behaviour of the Major Surfaces of Magnetite Fe3O4. *Phys. Chem. Chem. Phys.* 2014, *16*, 21082–21097.
(64) Wang, L.; Maxisch, T.; Ceder, G. Oxidation Energies of Transition Metal Oxides within the GGA+U Framework. *Phys. Rev. B* 2006, *73* (19), 195107.1-195107.6.
(65) Izumi, F.; Momma, K. Three-Dimensional Visualization in Powder Diffraction. *Solid State Phenom.* 2007, *130*, 15–20.
(66) Momma, K.; Izumi, F. VESTA 3 for Three-Dimensional Visualization of Crystal, Volumetric and Morphology Data. *J. Appl. Crystallogr.* 2011, *44*, 1272–1276.
(67) Matsui, M.; Tōdō, S.; Chikazumi, S. Magnetization of Low Temperature Phase of Fe3O4. *J. Phys. Soc. Japan* 1977, *43* (1), 47–52.

(68) Bengtson, A.; Morgan, D.; Becker, U. Spin State of Iron in Fe3O4 Magnetite and H-Fe3O4. *Phys. Rev. B - Condens. Matter Mater. Phys.* **2013**, *87* (15), 1–13.
(69) Roth, W. L. Magnetic Structures of MnO, FeO, CoO, and NiO. *Phys. Rev.* **1958**, *110* (6), 1333–1341.
(70) Fjellvåg, H.; Hauback, B. C.; Vogt, T.; Stølen, S. Monoclinic Nearly Stoichiometric Wüstite at Low Temperatures. *Am. Mineral.* **2002**, *87* (2–3), 347–349.
(71) Fischer, G.; Däne, M.; Ernst, A.; Bruno, P.; Lüders, M.; Szotek, Z.; Temmerman, W.; Hergert, W. Exchange Coupling in Transition Metal Monoxides: Electronic Structure Calculations. *Phys. Rev. B* **2009**, *80* (1), 014408.1-014408.11.
(72) Barré, M.; Catti, M. Neutron Diffraction Study of the B′ and γ Phases of LiFeO2. *J. Solid State Chem.* **2009**, *182* (9), 2549–2554.
(73) Anderson, J. C.; Dey, S. K.; Halpern, V. The Magnetic Susceptibilities of LiFeO2. *J. Phys. Chem. Solids* **1965**, *26* (9), 1555–1560.
(74) Grau-Crespo, R.; Hamad, S.; Catlow, C. R. A.; Leeuw, N. H. De; de Leeuw, N. H. Symmetry-Adapted Configurational Modelling of Fractional Site Occupancy in Solids. *J. Phys. Condens. Matter* **2007**, *19* (25), 256201.1-256201.16.
(75) Ong, S. P.; Richards, W. D.; Jain, A.; Hautier, G.; Kocher, M.; Cholia, S.; Gunter, D.; Chevrier, V. L.; Persson, K. A.; Ceder, G. Python Materials Genomics (Pymatgen): A Robust, Open-Source Python Library for Materials Analysis. *Comput. Mater. Sci.* **2013**, *68*, 314–319.
(76) Hart, G. L. W.; Forcade, R. W. Algorithm for Generating Derivative Structures. *Phys. Rev. B* **2008**, *77* (22), 224115.1-224115.12.
(77) Verwey, E. J. W. Electronic Conduction of Magnetite (Fe3O4) and Its Transition Point at Low Temperatures. *Nature* **1939**, *144* (3642), 327–328.
(78) Verwey, E. J. W.; Haayman, P. W. Electronic Conductivity and Transition Point of Magnetite (“Fe3O4”) . *Phys. Rev. B* **1941**, *8* (9), 979–987.
(79) Tang, J.; Wang, K.; Zhou, W. Magnetic Properties of Nanocrystalline Fe 3 O 4 Films Magnetic Properties of Nanocrystalline Fe 3 O 4 Films. **2014**, *7690* (2001), 9–12.
(80) Jeng, H.-T.; Guo, G. Y.; Huang, D. J. Charge-Orbital Ordering and Verwey Transition in Magnetite. *Phys. Rev. Lett.* **2004**, *93* (15), 156403.1-156403.4.
(81) Wright, J. P.; Attfield, J. P.; Radaelli, P. G. Long Range Charge Ordering in Magnetite below the Verwey Transition. *Phys. Rev. Lett.* **2001**, *87* (26), 266401.1-266401.4.
(82) Islam, M. S.; Fisher, C. A. J. Lithium and Sodium Battery Cathode Materials: Computational Insights into Voltage, Diffusion and Nanostructural Properties. *Chem. Soc. Rev.* **2014**, *43* (1), 185–204.
(83) Meng, Y. S.; Arroyo-de Dompablo, M. E. First Principles Computational Materials Design for Energy Storage Materials in Lithium Ion Batteries. *Energy Environ. Sci.* **2009**, *2* (6), 589–609.
(84) Urban, A.; Seo, D.-H.; Ceder, G. Computational Understanding of Li-Ion Batteries. *npj Comput. Mater.* **2016**, *2* (1), 16002.1-16002.13.
(85) Saal, J. E.; Kirklin, S.; Aykol, M.; Meredig, B.; Wolverton, C. Materials Design and Discovery with High-Throughput Density Functional Theory: The Open Quantum Materials Database (OQMD). *JOM* **2013**, *65* (11), 1501–1509.
(86) Kirklin, S.; Saal, J. E.; Meredig, B.; Thompson, A.; Doak, J. W.; Aykol, M.; Rühl, S.; Wolverton, C. The Open Quantum Materials Database (OQMD): Assessing the Accuracy of

DFT Formation Energies. *npj Comput. Mater.* 2015, *1* (1), 1–15.
(87) Jain, A.; Hautier, G.; Ong, S. P.; Moore, C. J.; Fischer, C. C.; Persson, K. A.; Ceder, G. Formation Enthalpies by Mixing GGA and GGA + U Calculations. *Phys. Rev. B* 2011, *84* (4), 045115.1-045115.10.
(88) Stevanović, V.; Lany, S.; Zhang, X.; Zunger, A. Correcting Density Functional Theory for Accurate Predictions of Compound Enthalpies of Formation: Fitted Elemental-Phase Reference Energies. *Phys. Rev. B* 2012, *85* (11), 115104.1-115104.12.
(89) Seo, D.-H.; Urban, A.; Ceder, G. Calibrating Transition-Metal Energy Levels and Oxygen Bands in First-Principles Calculations: Accurate Prediction of Redox Potentials and Charge Transfer in Lithium Transition-Metal Oxides. *Phys. Rev. B* 2015, *92* (11), 115118.1-115118.11.
(90) Chase, M.W., J. NIST-JANAF Themochemical Tables. *J. Phys. Chem. Ref. Data* 1998, *Monograph*, 1–1951.
(91) O. Kubaschewski, C. B. Alcock, P. J. S. Materials Thermochemistry. In *Materials Thermochemistry*; Pergamon Press: Oxford, UK, 1993; pp 257–323.
(92) Majzlan, J.; Navrotsky, A.; Schwertmann, U. Thermodynamics of Iron Oxides: Part III. Enthalpies of Formation and Stability of Ferrihydrite (∼Fe(OH)3), Schwertmannite (∼FeO(OH)3/4(SO4)1/8), and ε-Fe2O3. *Geochim. Cosmochim. Acta* 2004, *68* (5), 1049–1059.
(93) Andersson J.O., Helander T., Höglund L., Shi P.F., and S. B. Thermo-Calc and DICTRA, Computational Tools for Materials Science. SSBU Database. *Calphad* 2002, *26*, 273–312.
(94) Menard, M. C.; Marschilok, A. C.; Takeuchi, K. J.; Takeuchi, E. S. Variation in the Iron Oxidation States of Magnetite Nanocrystals as a Function of Crystallite Size: The Impact on Electrochemical Capacity. *Electrochim. Acta* 2013, *94* (42), 320–326.
(95) Li, Y. Private Communication: Unpublished DFT Results for Two Formula Unit Cell LiFe3O4 Structures. 2016.
(96) Shafi, K. V. P. M.; Ulman, A.; Dyal, A.; Yan, X.; Yang, N.-L.; Estournès, C.; Fournès, L.; Wattiaux, A.; White, H.; Rafailovich, M. Magnetic Enhancement of γ-Fe2O3 Nanoparticles by Sonochemical Coating. *Chem. Mater.* 2002, *14* (4), 1778–1787.
(97) Wang, J.; Ma, Y.; Watanabe, K. Magnetic-Field-Induced Synthesis of Magnetic γ-Fe2O3 Nanotubes. *Chem. Mater.* 2008, *20* (1), 20–22.
(98) Berkowitz, A. E.; Schuele, W. J.; Flanders, P. J. Influence of Crystallite Size on the Magnetic Properties of Acicular γ-Fe2O3 Particles. *J. Appl. Phys.* 1968, *39* (2), 1261–1263.
(99) Shepherd, J. P.; Koenitzer, J. W.; Aragón, R.; Spal/ek, J.; Honig, J. M. Heat Capacity and Entropy of Nonstoichiometric Magnetite Fe3(1−δ)O4. *Phys. Rev. B* 1991, *43* (10), 8461–8471.

For Table of Contents Only

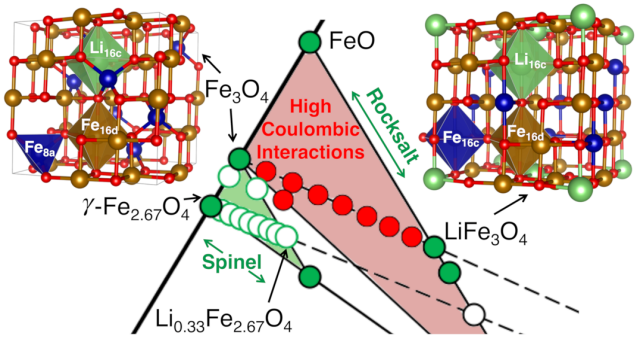

Supplementary Information

Energetics of Lithium Insertion into Magnetite, Defective Magnetite, and Maghemite

Christianna N. Lininger[a], Christina A. Cama[b,#], Kenneth J. Takeuchi[b,c], Amy C. Marschilok[b,c], Esther S. Takeuchi[b,c,d], Alan C. West[a,e], Mark S. Hybertsen[f,*]

[a]Department of Chemical Engineering, Columbia University, New York, NY, 10027, United States

[b]Department of Chemistry, Stony Brook University, Stony Brook, NY, 11794, United States

[c]Department of Material Science and Engineering, Stony Brook University, Stony Brook, NY, 11794, United States

[d]Energy and Photon Sciences Directorate, Brookhaven National Laboratory, Upton, NY, 11973, United States

[e] Department of Earth and Environmental Engineering, Columbia University, New York, NY, 10027, United States

[f]Center for Functional Nanomaterials, Brookhaven National Laboratory, Upton, NY, 11973, United States

[#] Current address: Department of Chemistry, St. Cloud State University, St. Cloud, MN 56301-4498

*Email: mhyberts@bnl.gov

Contents

1. Fe_3O_4 Charge and Orbital Ordering Tests

2. $LiFe_3O_4$ Charge Ordering Tests

3. Li-Fe-O Ternary Phase Diagram

4. Additional Tables and Figures

Table S1. Supercell specifications and k-point sampling.

Table S2. DFT+U predicted structural properties for Li-Fe-O ternary phases.

Table S3. Enumeration of configurations for $Li_xFe_3O_4$ in an eight formula unit cell.

Table S4. Formation energies for known compounds in the Li-Fe-O phase diagram.

Figure S1. Formation energy of $Li_{0.5}Fe_3O_4$ as a function of the U_{eff} in DFT+U.

Figure S2. Energies for selective sampling of $Li_xFe_3O_4$ configurations.

Figure S3. Magnetite structures with charge and orbital ordering.

Figure S4. Charge Order in $LiFe_3O_4$.

Figure S5. Structure visualization: $LiFe_3O_4$, $Li_{1.125}Fe_{2.875}O_4$, and $Li_{1.33}Fe_{2.67}O_4$.

5. Lowest Energy $LiFe_3O_4$ structure: CIF format

1. Fe_3O_4 Charge and Orbital Ordering Tests. The present study was primarily based on the eight formula unit cell determined by starting from the room temperature, Fd$\bar{3}$m cell. As noted in the main text, the relaxed structure showed the Verwey charge order for the eight Fe^{2+} and eight Fe^{3+} formal cations on the 16d sites, visualized in Fig. S3(a). In a local picture, the extra electron for each Fe^{2+} cation would partially occupy a spin down, three-fold-degenerate t_{2g} manifold for full octahedral symmetry. As discussed in the text, full relaxation included Jahn-Teller driven distortions locally that lifted this degeneracy. We examined the local, projected orbital character of the electronic states on the Fe^{2+} sites and in the minority spin channel. A manifold of eight states in the local, minority spin down channel were the highest occupied states and they showed predominantly equal projections on dyz and dxz character. Correspondingly, the unit cell relaxed to one with an elongated c =8.60 Å cell parameter and a=b=8.50 Å. These results agree with those reported by Zhou and Ceder for this unit cell with Verwey charge order.[1]

Another charge order was tested by starting from the P2/c cell with eight formula units and atomic positions fitted to experiments at 90 K by Wright, et al.[2] The charge and orbital order is illustrated in Fig. S.3(b) for the final, fully relaxed structure (a=6.04 Å, b=6.06 Å, and c=17.01 Å). Here, the charge order in the [0, 0, 1] direction showed a sequence where the first plane was Fe^{2+}, the second plane was comprised of 50:50 Fe^{2+}: Fe^{3+}, the third plane was all Fe^{3+}, and the fourth plane was 50:50 Fe^{2+}: Fe^{3+}. This charge order agrees with that found by Jeng, Guo, and Huang.[3] As noted in the main text, we found this structure to be higher in energy than our Fd$\bar{3}$m derived structure by 0.002 eV/f.u. For comparison, Zhou and Ceder[1] report an energy that is higher by 0.007 eV/f.u., similar to our result. Examining the projected, occupied minority spin orbitals on the Fe^{2+} sites, the layers comprised of only Fe^{2+} showed dxz orbital occupation and the mixed layers showed dxy orbital occupation. Jeng, Guo, and Huang saw a similar pattern of alternation of the orbitals between the layers, but within the Fe^{2+} layers, they found an additional patter of alternation between dxz and dyz.[3] There was more than one unique Fe^{2+} octahedron. In the highest symmetry ones, we found the bond lengths formed a pattern of four long (2.17 to 2.18 Å) and two short (2.09 Å) Fe-O bond lengths. The lower symmetry Fe^{2+} octahedra had long bonds ranging from 2.14 to 2.17 Å and short bonds at 2.07 Å. This was very similar to the initial experimental structure and that found by Jeng, Guo, and Huang. Among the smaller, Fe^{3+} octahedra, there was essentially no symmetry, but generally we found two groups of bond lengths, three shorter (2.00 to 2.02 A) and three longer (2.08 to 2.11 Å), similar to the initial experimental structure, but differing from the prior calculation (four longer and two shorter).

Finally, we considered a P2/m cell with four formula units. It was set to the equilibrium volume determined by the fully relaxed Fd$\bar{3}$m cell, allowed to relaxed internally only, fixing cell shape and size (a=b=6.05 Å and c=8.50 Å). This was done to isolate single orbital occupancy in this cell shape. This case resulted in Verwey charge order and occupancy of just the dxz orbital on the Fe^{2+} sites, Fig. S3(c). The energy was found to be 0.011 eV/f.u. higher than our Fd$\bar{3}$m derived structure. The orbital order and the energy difference agree Zhou and Ceder who also report 0.011 eV/f.u.[1]

2. $LiFe_3O_4$ Charge Order. The u_{iso} value provides a measure capturing the internal distortions of the oxygen framework compatible with the high temperature cubic phase. A u_{iso} value of 0.0 corresponds to the highest symmetry positions for all oxygen and results in all octahedra in the cell having identical volume. For the 97 $LiFe_3O_4$ calculations performed herein, a value of $u_{iso,exp}$ = 0.004 (from Fe_3O_4 experiment) was imposed, unless otherwise specified. This value of u_{iso} biases all 16c sites to have an expanded polyhedra over the 16d sites, favoring the larger Fe^{2+} on the 16c site. A negative value of u_{iso} flips the bias, favoring 16c to be comprised of Fe^{3+}.

To test the role of the initial choice of positive u_{iso} and the robustness of Fe^{2+} on the 16c sites, 13 specific Li:Fe configurations were fully relaxed from a starting u_{iso} of -2* $u_{iso,exp}$. The 13 ionic orders were the lowest 10 structures, the highest energy structure #97, and intermediate structures #48 and #78, as ranked in energy. Following full relaxation, the structures were then compared to the same Li:Fe configurations that had been relaxed from the starting experimental u_{iso} value. For these two starting structures, as modulated by $u_{iso,exp}$ or -2*$u_{iso,exp}$, the self-consistent charge order was representative of the volume effects imposed by the starting value of u_{iso}. Namely, the effect of the negative u_{iso} value, decreasing 16c octahedra volume compared to 16d, was largely maintained throughout the relaxation. On average, 75% of the 16c irons relaxed to

Fe^{3+}. For comparison, using the positive, experimental u_{iso} value, 100% of the 16c irons relaxed to Fe^{2+}.

Of the 13 Li:Fe 16c cation order arrangements tested, the root mean square energy difference between the two charge orders driven by choice of u_{iso} was 0.033 eV/f.u. For comparison, the range of energy covered by the 13 Li:Fe 16c selected structures based on Li cation order was ~0.16 eV/f.u. To supplement Fig. 6a in the main text, the formation energy for all 13 structures tested with the $-2*u_{iso,exp}$ starting point are added to the plot and shown in Fig. S4c. To further illustrate the changes found in these tests of charge ordering, Fig. S4d, shows a data point for each unique Li cation order tested. The x-axis is the fully relaxed energy from the $-2*u_{iso,exp}$ starting point and the y-axis is the fully relaxed energy from the $u_{iso,exp}$ starting point. It can be seen that for 10 of the 13 Li cation configurations tested, the $u_{iso,exp}$ starting point relaxed to the lowest energy charge order.

3. Li-Fe-O Ternary Phase Diagram. Here we detail the experimental and computed formation energies for structures used in Li-Fe-O ternary phase diagram (Fig. 1) and the methodology for empirical corrections to DFT+U formation energies. The summary of the final information appears in Table S4. All experimental values are at standard conditions unless otherwise noted. Theoretical formation energies are from the Open Quantum Materials Database (OQMD)[4], the Materials Project Database[5], and the theoretical formation energies computed here.

All structures in Table S4, except those for FeO, $LiFeO_2$, and α-Fe_2O_3, were obtained from Materials Project Database and fully relaxed with methods described in Sect. 2.2 and in Table S1. The two corrections applied to the DFT+U results are related to the formation energy of O_2 and mixing of GGA with GGA+U calculations for calculation of reaction energies where appropriate. Previously, the correction for O_2 has been found to be a constant shift in the O_2 formation energy by Wang, et al. [6] The second correction traces to the basic idea that GGA gives better overall reaction energies or predictions of stability for metals while GGA+U gives better results for transition metal oxides. When both cases are involved in a reaction energy, e.g., BCC-Fe and iron oxides, a scheme has been developed using appropriate thermodynamic cycles to correct the reaction energies that scales with the amount of metal reduction.[7] To capture both of these corrections for the dataset encapsulated by the Li-Fe-O ternary phase diagram, we have used a two-parameter least-squares regression to all the data in Table S4, unless denoted with an asterisk. With this regression, we have fit 1.06 eV/O_2 and 2.47 eV/Fe. For comparison, the previously published corrections, determined by fitting to a broader set of data at a different Ueff (4.0 eV for Fe) were 1.36 eV/O_2[6] and 1.723 eV/Fe.[7] Our formation energies without and with corrections are shown in the 5th and 6th columns of Table S4 respectively.

4. Additional Figures and Tables

Table S1. Supercell specifications and k-point sampling. Except where noted, the supercells are nominally cubic. For cases where variable amounts of Li are indicated, the volume per cell is for the parent compound with x=0.

Compound	Number of Formula Units	Volume per oxygen (Å^3)	K-point Sampling
$Li_xFe_3O_4$	8	19.44 Å^3	3x3x3
$Li_xFe_3O_4$	16[a]	19.44 Å^3	2x2x2
$Li_xFe_{2.875}O_4$	8	19.27 Å^3	3x3x3
$Li_xFe_{2.667}O_4$	24[b]	18.94 Å^3	3x3x1
Li^0	2	40.41 Å^3	7x7x7
FeO	32	21.09 Å^3	3x3x3
α-Fe_2O_3	6[c]	23.97 Å^3	4x4x4
$LiFeO_2$	16	18.74 Å^3	3x3x3
LiO	4[d]	16.53 Å^3	8x8x3
Li_2O	32	27.40 Å^3	3x3x3
Li_5FeO_4	8	24.66 Å^3	3x3x3
$LiFe_5O_8$	4	18.72 Å^3	3x3x3

a Rhombohedral
b Tetragonal
c Monoclinic
d Hexagonal

Table S2. DFT+U predicted structural properties for Li-Fe-O ternary phases. Predicted structural properties for the stable phases examined in the Li-Fe-O ternary phase diagram.

	Lattice Parameters: a, b, c in Å α, β, γ in degree	Local Fe Magnetic Moments (m_b/Fe), Multiplicity (Wyckoff Site in Fd$\bar{3}$m, where appropriate)
Fe_3O_4 Inverse Spinel	8.50, 8.50, 8.60 90.00, 90.00, 90.69	-4.2, 8 (8a) 4.3, 8 (16d) 3.7, 8 (16d)
$Fe_{2.875}O_4$ Inverse Spinel	8.52, 8.52, 8.50 89.74, 90.26, 89.94	-4.2, 8 (8a) 4.3, 10 (16d) 3.7, 5 (16d)
$Fe_{2.667}O_4$ Maghemite	8.47, 8.47, 25.35 90.00, 90.00, 90.00	-4.2, 24 (8a) 4.3, 48 (16d)
FeO	8.68, 8.68, 8.97 90.17, 90.17, 88.28	3.73, 16 -3.73, 16
α-Fe_2O_3	8.23, 8.24, 9.50 54.78, 125.24, 109.71	4.3, 8 -4.3, 8
$LiFeO_2$	8.43, 8.45, 8.43 89.90, 89.84, 89.90	4.3, 8 -4.3, 8
LiO	3.15, 3.15, 7.68 90.00, 90.00, 120.00	-
Li_2O	9.23, 9.23, 9.23 90.00, 90.00, 90.00	-
Li_5FeO_4	9.21, 9.25, 9.26 90.00, 90.00, 90.00	4.2, 8
$LiFe_5O_8$	8.43, 8.43, 8.43 90.00, 90.00, 90.00	-4.2, 8 4.3, 12

Table S3. Enumeration of configurations for $Li_xFe_3O_4$ in an eight formula unit cell. Total number and unique number of configurations for $Li_xFe_3O_4$ in an eight formula unit cell for the spinel parent with Li atoms and vacancies (V) on 16c (columns 2-3) and the rock-salt parent with the eight Fe atoms, Li atoms and vacancies (V) on 16c (columns 4-5). Symmetry of the parent compound was applied in each case without regard for charge or orbital order among the Fe^{2+} and Fe^{3+} on the fully occupied 16d sites.

	Spinel 16c: Li_nV_{16-n}		Rock-salt 16c: $Fe_8Li_nV_{8-n}$	
Li number (concentration)	Total	Unique	Total	Unique
1 (0.125)	16	1	102,960	580
2 (0.250)	120	3	360,360	1,995
3 (0.375)	560	8	720,720	3,885
4 (0.500)	1,820	22	900,900	4,879
5 (0.625)	4,368	35	720,720	3,885
6 (0.750)	8008	65	360,360	1,995
7 (0.875)	11,440	82	102,960	580
8 (1.000)	12,870	97	12,870	97

Table S4. Formation energies for known compounds in the Li-Fe-O phase diagram. Note that these phases appear in the same order in the table below as they are plotted in Fig. 3 in the main text, except that results for γ-Fe_2O_3 are not plotted and the data for $LiFeO_2$ naturally appears twice as the path through the phase diagram followed in Fig. 3 crosses there.

Compound	Experimental ΔH (eV/atom)	Theory from Materials Project (eV/atom)	Theory from OQMD Database (eV/atom)	Computed with DFT +U (eV/atom)	Computed with Corrections (eV/atom)	Materials Project Material Id
LiO	-1.65[8]	-1.65	-1.62	-1.45	-1.71	mp-841
$LiFeO_2$	-1.94[9]	-2.08	-1.93	-2.03	-1.93	mp-851027
FeO	-1.42[8]	-1.67	-1.52	-1.92	-1.46	mp-715262
Fe_3O_4	-1.67[8]	-1.84	-1.64	-1.97	-1.66	mp-19306
α-Fe_2O_3	-1.72[8]	-1.89	-1.65	-1.97	-1.71	mp-715572
γ-Fe_2O_3*	-1.68[10]	-	-	-1.94	-1.68	-
$LiFe_5O_8$	-1.80[9]	-1.90	-1.73	-2.00	-1.79	mp-31768
Li_5FeO_4	-2.04[9]	-2.1	-2.00	-1.97	-2.04	mp-19511
Li_2O	-2.08[8]	-2.07	-1.98	-1.88	-2.05	mp-1960

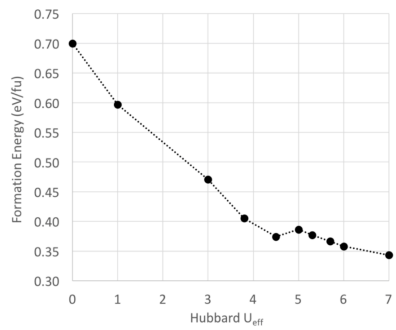

Figure S1. Formation energy of $Li_{0.5}Fe_3O_4$ as a function of the U_{eff} in DFT+U. To probe the effect of the Hubbard U parameter on the formation energy of lithiated iron oxides, the formation energy of $Li_{0.5}Fe_3O_4$ was calculated relative to Fe_3O_4 and $LiFe_3O_4$ in two formula unit cells for a broad range of values of U_{eff}. In the range of U_{eff} = 4.5 - 5.3 eV, the formation energy was found to vary by less than 0.03 eV/f.u.

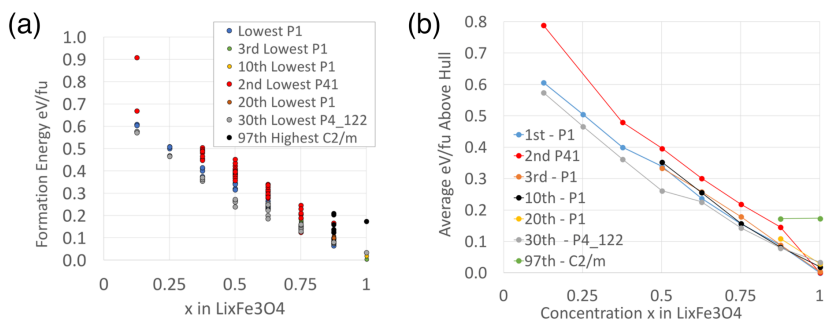

Figure S2. Energies for selective sampling of $Li_xFe_3O_4$ configurations. Calculated formation energies for $Li_xFe_3O_4$ relative to Fe_3O_4 and $Li_1Fe_3O_4$. As described in Sect. 2.3, the configurations considered start from a sampling of the 97 configurations for $Li_1Fe_3O_4$, rank ordered from lowest energy (1st, 2nd, 3rd, 10th, 20th, 30th, and 97th). All symmetry distinct configurations for formation of a Li vacancy were considered initially for x=1. For the lowest energy configuration at x=0.875, the symmetry distinct configurations for another Li vacancy were considered. The sequence was followed then to lower Li concentration as needed. (a) All calculated formation energies are shown. (b) The average energy above the convex hull is shown for all structures with a unique 16c Li:Fe parent cation order.

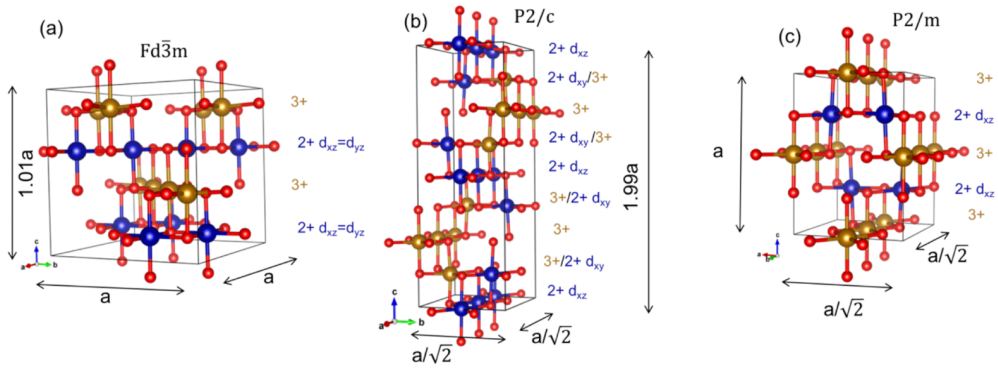

Figure S3. Magnetite structures with charge and orbital ordering. Spinel structure showing the 32e O atoms and the 16d octahedral Fe atoms but suppressing the 8a tetrahedral Fe atoms for clarity. (a) Fully relaxed lowest energy charge and orbital order, found starting from the room temperature, Fd$\bar{3}$m eight formula unit cell. (b) Fully relaxed, lowest energy charge and orbital order found starting from a measured, low temperature P2/c eight formula unit cell determined by Wright, et al.[2] Alternative experimental charge order found by Wright et al. and fully relaxed herein. (c) P2/m cell with fixed cell parameters but allowed to fully relax internally.

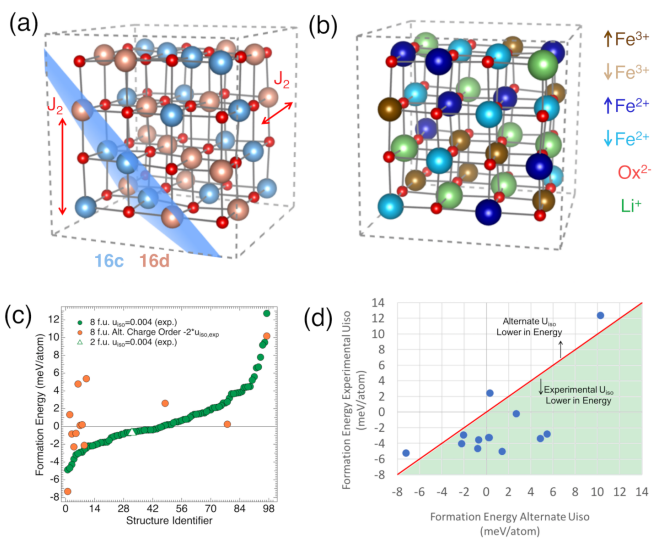

Figure S4. Charge Order in $LiFe_3O_4$. (a) The relationship between the 16c and 16d sites in the Fd$\bar{3}$m space group in an eight formula unit cell. The 16c sites are shown in blue and the 16d sites are shown in peach. The second nearest neighbor spin-spin interaction between cations, J_2, between the 16c and 16d sites is illustrated by the red arrows. (b) Charge order found self-consistently for the lowest energy configuration of Li cations and using the positive $u_{iso,exp}$ starting point. For comparison, the charge order found self-consistently for the same Li cation configuration and using the -2*$u_{iso,exp}$ starting point is shown in Fig. 7a of the main text. (c) Recapitulation of Fig. 6a from the main text showing the formation of as a function of Li cation distribution in the eight formula unit cell with the addition of all 13 cases considered with the -2*u_{iso} starting point (orange). (d) Each data point corresponds to the same Li cation configuration, covering the 13 test cases probing the stability of Fe^{2+} versus Fe^{3+} on 16c. The x-axis is the formation energy for the fully relaxed structure from the -2*$u_{iso,exp}$ starting point, and the y-axis is the formation energy from the positive $u_{iso,exp}$ starting point.

Figure S5. Structure visualization: $LiFe_3O_4$, $Li_{1.125}Fe_{2.875}O_4$, and $Li_{1.33}Fe_{2.67}O_4$. Fully relaxed structures for the lowest energy configurations found for (a) $LiFe_3O_4$, (b) $Li_{1.125}Fe_{2.875}O_4$, and (c) $Li_{1.33}Fe_{2.67}O_4$.

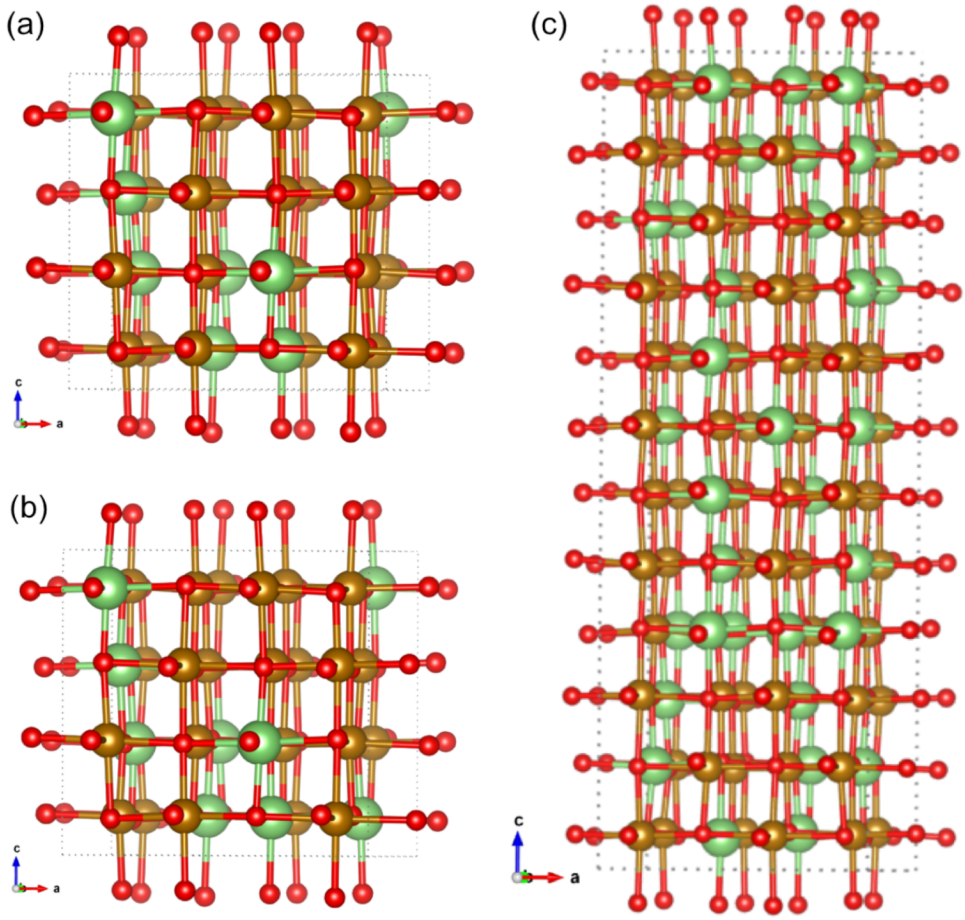

5. $LiFe_3O_4$ Lowest Energy Structure File

```
_chemical_name_common          'LiFe3O4 Lowest Energy Structure'
_cell_length_a                 8.61394
_cell_length_b                 8.65190
_cell_length_c                 8.55383
_cell_angle_alpha              89.82958
_cell_angle_beta               90.04173
_cell_angle_gamma              89.76738
_space_group_name_H-M_alt      'P 1'
_space_group_IT_number         1
loop_
_space_group_symop_operation_xyz
  'x, y, z'
loop_
  _atom_site_label
  _atom_site_occupancy
  _atom_site_fract_x
  _atom_site_fract_y
  _atom_site_fract_z
  _atom_site_adp_type
  _atom_site_B_iso_or_equiv
  _atom_site_type_symbol
  Fe1    1.0   0.500777   0.502624   0.498726   Biso  1.000000 Fe
  Fe2    1.0   0.250670   0.751804   0.002879   Biso  1.000000 Fe
  Fe3    1.0   0.746381   0.001983   0.252608   Biso  1.000000 Fe
  Fe4    1.0   0.003818   0.249395   0.752755   Biso  1.000000 Fe
  Fe5    1.0   0.753246   0.250343   0.001826   Biso  1.000000 Fe
  Fe6    1.0   0.250619   0.000192   0.744624   Biso  1.000000 Fe
  Fe7    1.0   0.999675   0.752048   0.250213   Biso  1.000000 Fe
  Fe8    1.0   0.496981   0.001278   0.003056   Biso  1.000000 Fe
  Fe9    1.0   0.252677   0.250339   0.502107   Biso  1.000000 Fe
  Fe10   1.0   0.748863   0.495474   0.748201   Biso  1.000000 Fe
  Fe11   1.0   0.742340   0.748739   0.492572   Biso  1.000000 Fe
  Fe12   1.0   0.252350   0.502672   0.251453   Biso  1.000000 Fe
  Fe13   1.0   0.003918   0.497539   0.000020   Biso  1.000000 Fe
  Fe14   1.0   0.502788   0.249497   0.254421   Biso  1.000000 Fe
  Fe15   1.0   0.494067   0.750786   0.745923   Biso  1.000000 Fe
  Fe16   1.0   0.999147   0.999152   0.500593   Biso  1.000000 Fe
  Fe17   1.0   0.498639   0.249478   0.749062   Biso  1.000000 Fe
  Fe18   1.0   0.000136   0.500731   0.502062   Biso  1.000000 Fe
  Fe19   1.0   0.749598   0.749041   0.004708   Biso  1.000000 Fe
  Fe20   1.0   0.251683   0.999178   0.255145   Biso  1.000000 Fe
  Fe21   1.0   0.748643   0.003496   0.747096   Biso  1.000000 Fe
```

Fe22	1.0	0.001619	0.747842	0.749134	Biso	1.000000	Fe
Fe23	1.0	0.999723	0.248056	0.247908	Biso	1.000000	Fe
Fe24	1.0	0.500639	0.498760	0.998679	Biso	1.000000	Fe
O1	1.0	0.261019	0.257834	0.244181	Biso	1.000000	O
O2	1.0	0.488776	0.008829	0.746681	Biso	1.000000	O
O3	1.0	0.984744	0.754308	0.493364	Biso	1.000000	O
O4	1.0	0.742564	0.511366	0.002283	Biso	1.000000	O
O5	1.0	0.014320	0.490019	0.257918	Biso	1.000000	O
O6	1.0	0.757449	0.746570	0.740969	Biso	1.000000	O
O7	1.0	0.508760	0.245956	0.010375	Biso	1.000000	O
O8	1.0	0.250086	0.995914	0.502313	Biso	1.000000	O
O9	1.0	0.506503	0.014444	0.255918	Biso	1.000000	O
O10	1.0	0.006990	0.243704	0.509442	Biso	1.000000	O
O11	1.0	0.260150	0.514210	0.009780	Biso	1.000000	O
O12	1.0	0.007123	0.487295	0.742423	Biso	1.000000	O
O13	1.0	0.490366	0.756338	0.989997	Biso	1.000000	O
O14	1.0	0.745462	0.986591	0.499381	Biso	1.000000	O
O15	1.0	0.240242	0.763713	0.760803	Biso	1.000000	O
O16	1.0	0.493563	0.489077	0.257002	Biso	1.000000	O
O17	1.0	0.995003	0.257876	0.990839	Biso	1.000000	O
O18	1.0	0.007360	0.009708	0.753805	Biso	1.000000	O
O19	1.0	0.741516	0.237926	0.255474	Biso	1.000000	O
O20	1.0	0.507054	0.738339	0.504928	Biso	1.000000	O
O21	1.0	0.494246	0.489944	0.738761	Biso	1.000000	O
O22	1.0	0.009233	0.739454	0.007007	Biso	1.000000	O
O23	1.0	0.987755	0.008846	0.247688	Biso	1.000000	O
O24	1.0	0.497671	0.264736	0.492373	Biso	1.000000	O
O25	1.0	0.761711	0.251717	0.744646	Biso	1.000000	O
O26	1.0	0.261318	0.505600	0.488803	Biso	1.000000	O
O27	1.0	0.253411	0.742359	0.242017	Biso	1.000000	O
O28	1.0	0.750733	0.990319	0.001303	Biso	1.000000	O
O29	1.0	0.741368	0.513209	0.492309	Biso	1.000000	O
O30	1.0	0.246884	0.986791	0.003852	Biso	1.000000	O
O31	1.0	0.743810	0.766746	0.257197	Biso	1.000000	O
O32	1.0	0.240906	0.234727	0.757371	Biso	1.000000	O
Li1	1.0	0.003897	0.003439	0.000300	Biso	1.000000	Li
Li2	1.0	0.748150	0.252458	0.497339	Biso	1.000000	Li
Li3	1.0	0.251361	0.498564	0.747567	Biso	1.000000	Li
Li4	1.0	0.497895	0.752568	0.256063	Biso	1.000000	Li
Li5	1.0	0.261140	0.749730	0.494710	Biso	1.000000	Li
Li6	1.0	0.746183	0.497193	0.249923	Biso	1.000000	Li
Li7	1.0	0.246802	0.246337	0.999232	Biso	1.000000	Li
Li8	1.0	0.497477	0.994799	0.497893	Biso	1.000000	Li

Supplementary Information References

(1) Zhou, F.; Ceder, G. First-Principles Determination of Charge and Orbital Interactions in Fe3O4. *Phys. Rev. B - Condens. Matter Mater. Phys.* 2010, *81* (20), 3–8.

(2) Wright, J. P.; Attfield, J. P.; Radaelli, P. G. Charge Ordered Structure of Magnetite Fe3O4 below the Verwey Transition. *Phys. Rev. B* 2002, *66* (21), 214422.1-214422.15.

(3) Jeng, H.-T.; Guo, G. Y.; Huang, D. J. Charge-Orbital Ordering in Low-Temperature Structures of Magnetite: GGA+U Investigations. *Phys. Rev. B* 2006, *74* (19), 195115.1-195115.10.

(4) Kirklin, S.; Saal, J. E.; Meredig, B.; Thompson, A.; Doak, J. W.; Aykol, M.; Rühl, S.; Wolverton, C. The Open Quantum Materials Database (OQMD): Assessing the Accuracy of DFT Formation Energies. *npj Comput. Mater.* 2015, *1* (1), 1–15.

(5) Jain, A.; Ong, S. P.; Hautier, G.; Chen, W.; Richards, W. D.; Dacek, S.; Cholia, S.; Gunter, D.; Skinner, D.; Ceder, G.; Persson, K. A. Commentary: The Materials Project: A Materials Genome Approach to Accelerating Materials Innovation. *APL Mater.* 2013, *1* (1), 11002.1-11002.11.

(6) Wang, L.; Maxisch, T.; Ceder, G. Oxidation Energies of Transition Metal Oxides within the GGA+U Framework. *Phys. Rev. B* 2006, *73* (19), 195107.1-195107.6.

(7) Jain, A.; Hautier, G.; Ong, S. P.; Moore, C. J.; Fischer, C. C.; Persson, K. A.; Ceder, G. Formation Enthalpies by Mixing GGA and GGA + U Calculations. *Phys. Rev. B* 2011, *84* (4), 045115.1-045115.10.

(8) Chase, M.W., J. NIST-JANAF Themochemical Tables. *J. Phys. Chem. Ref. Data* 1998, *Monograph*, 1–1951.

(9) Andersson J.O., Helander T., Höglund L., Shi P.F., and S. B. Thermo-Calc and DICTRA, Computational Tools for Materials Science. SSBU Database. *Calphad* 2002, *26*, 273–312.

(10) Majzlan, J.; Navrotsky, A.; Schwertmann, U. Thermodynamics of Iron Oxides: Part III. Enthalpies of Formation and Stability of Ferrihydrite (∼Fe(OH)3), Schwertmannite (∼FeO(OH)3/4(SO4)1/8), and ε-Fe2O3. *Geochim. Cosmochim. Acta* 2004, *68* (5), 1049–1059.